Commun. Comput. Phys.
doi: 10.4208/cicp.OA-2016-0029

Vol. **21**, No. 3, pp. 718-747
March 2017

Projected Finite Elements for Systems of Reaction-Diffusion Equations on Closed Evolving Spheroidal Surfaces

Necibe Tuncer[1,*] and Anotida Madzvamuse[2]

[1] *Department of Mathematics, Florida Atlantic University, 777 Glades Road, Boca Raton, Fl 33431, USA.*
[2] *University of Sussex, School of MPS, Department of Mathematics, BN1 9QH, Brighton, UK.*

Received 18 February 2016; Accepted (in revised version) 20 July 2016

Abstract. The focus of this article is to present the projected finite element method for solving systems of reaction-diffusion equations on evolving closed spheroidal surfaces with applications to pattern formation. The advantages of the projected finite element method are that it is easy to implement and that it provides a conforming finite element discretization which is "logically" rectangular. Furthermore, the surface is not approximated but described exactly through the projection. The surface evolution law is incorporated into the projection operator resulting in a time-dependent operator. The time-dependent projection operator is composed of the radial projection with a Lipschitz continuous mapping. The projection operator is used to generate the surface mesh whose connectivity remains constant during the evolution of the surface. To illustrate the methodology several numerical experiments are exhibited for different surface evolution laws such as uniform isotropic (linear, logistic and exponential), anisotropic, and concentration-driven. This numerical methodology allows us to study new reaction-kinetics that only give rise to patterning in the presence of surface evolution such as the *activator-activator* and *short-range inhibition; long-range activation*.

AMS subject classifications: 65M12, 65M60, 35K57, 35K58, 9208

Key words: Time-dependent projection operators, projected finite elements, non-autonomous partial differential equations, reaction-diffusion systems, evolving surfaces, Turing *diffusively-driven* instability, pattern formation.

1 Introduction

Currently, there is a surge in modelling parabolic partial differential equations on evolving arbitrary complex surfaces [1, 8, 9, 12–14, 24, 25] partly due to the advances in tech-

*Corresponding author. *Email addresses:* ntuncer@fau.edu (N. Tuncer), a.madzvamuse@sussex.ac.uk (A. Madzvamuse)

 ©2017 Global-Science Press

https://doi.org/10.4208/cicp.OA-2016-0029 Published online by Cambridge University Press

niques for obtaining 3-dimensional datasets in experimental sciences [19]. Typical examples include molecular analysis of the fungus rice blast in plant biology [5], biochemical and biomechanical analysis of cell migration in cell motility [2, 35] and pattern formation in developmental biology [20, 23, 30]. In most cases, molecular species resident on the cell-surface are observed to react and diffuse and in doing so, induce surface evolution. Mathematical modelling of such processes results in highly nonlinear systems of reaction-diffusions equations posed on time-dependent closed (and sometimes open) surfaces or manifolds. The theory of reaction-diffusion is well-studied on stationary planar domains but not so much is known of the models on evolving planar domains and surfaces. Due to the nature of the nonlinearities, closed form solutions are not readily available. Furthermore, including surface evolution adds extra complexities to the model system in that non-autonomous systems of parabolic partial differential equations are obtained which render redundant standard theoretical analytical techniques such as the linear stability theory for analysing the model dynamics close to the bifurcation points [17, 27]. Hence it is critical to develop new numerical methodologies and techniques for solving, robustly and efficiently, systems of non-autonomous nonlinear parabolic partial differential equations on complex evolving surfaces.

To-date, there has been an increase in the development of numerical methods for approximating solutions of partial differential equations posed on evolving surfaces. Examples include (but are not limited to) the method of lines [4], evolving surface finite element methods on triangulated surfaces [1, 8, 9, 12, 13], implicit finite element methods using level set descriptions of the surfaces [11, 12, 33, 37], diffuse interface methods of which phase-fields are an example [3, 6, 14], particle methods using level set descriptions of the surface [7, 16, 18, 22] and closest-point methods [24, 25]. In all these methods the continuous surface is approximated by a discrete surface thereby committing a *geometrical error*. A key issue is how the surface description is encoded into the numerical method. For the evolving surface finite elements, the surface is approximated by a triangulated surface. The geometrical description of the surface is encoded through the knowledge of the vertices of the triangulation. A geometrical error is committed in carrying out the surface triangulation [13]. On the other hand, numerical methods based on implicit surfaces require the knowledge of the level set function that defines the surface geometry [13]. A key difference between these methods and the projected finite element method (PFEM) is that the latter does not commit geometric errors since the surface is not approximated but described exactly through the projection. The surface evolution is embedded into the projection operator.

The PFEM proposed in this article is inspired by the radially projected finite element method which was used to compute approximate numerical solutions for partial differential equations on stationary spheroidal surfaces such as spheres, ellipsoids, and tori [31, 38, 39]. The PFEM gives a geometrically exact discretization of spheroidal surfaces (the geometry is not approximated, but represented exactly) and is attractive for numerical simulations since the resulting finite element discretization is conforming and is "logically rectangular." The PFEM is easy to implement and incorporate into existing

https://doi.org/10.4208/cicp.OA-2016-0029 Published online by Cambridge University Press

finite element codes.

The structure of our article is as follows. Reaction-diffusion systems defined on arbitrary evolving spheroidal surfaces are formulated in Section 2. In this section we present appropriate notation and surface transport theorems to be used throughout the paper. For the interested reader, we present a brief derivation of the model equations on evolving surfaces. In Section 2.1 we present details of the projection operator and its generalisation to evolving surfaces. Within this section, we detail how the projection operator is exploited to generate the surface mesh and how surface evolution is embedded in the operator. A few examples are given to support the theoretical framework. For illustrative purposes, three nonlinear reactions are considered: the activator-depleted substrate model [15,34,36], the Gierer-Meinhardt model [15] and the non-standard *activator-activator* model [27]. The latter only gives rise to patterning in the presence of surface evolution. The main methodological derivation of the projected finite element method applied to evolving surfaces is presented in Section 3 and demonstrates how the method is used to generate the surface mesh triangulation describing the continuous surface. To illustrate the effectiveness, robustness and applicability of the projected finite elements, we perform several examples with uniform isotropic, anisotropic and concentration-driven surface evolution laws for the three nonlinear reaction kinetics outlined above. For each case we demonstrate how the surface evolution is embedded into the projection operator. For example, we show how patterns form when a sphere evolves continuously into either an ellipsoidal or dumbbell surface. This aspect is new and is presented for the first time in this article. Within this section we also point out the effects of surface evolution to the theory of pattern formation. Finally, in Section 5 we conclude and discuss our findings and lay down foundations for future research.

2 Models on evolving surfaces

In this paper, we consider reaction-diffusion systems defined on evolving surfaces. Let $\mathcal{S}(t)$ be an evolving two-dimensional closed surface embedded in $\mathbb{R}^3$ with a unit outward normal $\boldsymbol{n}$. Let $U(t)$ be any subset of $\mathbb{R}^3$ containing $\mathcal{S}(t)$. For any function $u(\boldsymbol{x})$ defined on $U(t)$,

$$u(\boldsymbol{x}):U(t)\to\mathbb{R},$$

we define its tangential derivative on $\mathcal{S}(t)$ as

$$\nabla_{\mathcal{S}(t)}u=\nabla u-(\nabla u\cdot\boldsymbol{n})\boldsymbol{n},$$

where $\boldsymbol{x}\cdot\boldsymbol{y}$ denotes the regular dot product for any $\boldsymbol{x}$ and $\boldsymbol{y}$ in $\mathbb{R}^3$, and ∇ denotes the regular gradient in $\mathbb{R}^3$. The tangential gradient is the projection of the regular gradient onto the tangent plane, thus

$$\nabla_{\mathcal{S}(t)}u\cdot\boldsymbol{n}=0.$$

https://doi.org/10.4208/cicp.OA-2016-0029 Published online by Cambridge University Press

The Laplace-Beltrami operator on the surface $\mathcal{S}(t)$ is defined to be the tangential divergence of the tangential gradient

$$\Delta_{\mathcal{S}(t)}u=\nabla_{\mathcal{S}(t)}\cdot\nabla_{\mathcal{S}(t)}u,$$

where the tangential divergence for the vector valued function $\boldsymbol{u}=(u_1,u_2,u_3)$ is defined as

$$\nabla_{\mathcal{S}(t)}\cdot\boldsymbol{u}=\nabla\cdot\boldsymbol{u}-\sum_{i=1}^{3}\Big(\nabla u_i\cdot\boldsymbol{n}\Big)n_i.$$

Suppose $\mathcal{S}(t)$ has a boundary $\partial\mathcal{S}$ whose unit outer normal tangential to $\mathcal{S}$ is denoted by $\boldsymbol{\mu}$ (known as the co-normal), and let $\boldsymbol{q}=(q_1,q_2,q_3)$ be a vector field in $\mathbb{R}^3$ (not necessarily tangent to the surface). Then the divergence theorem on the surface $\mathcal{S}(t)$ is given as follows

$$\int_{\mathcal{S}(t)}\nabla_{\mathcal{S}(t)}\cdot\boldsymbol{q}=\int_{\partial\mathcal{S}(t)}\boldsymbol{q}\cdot\boldsymbol{\mu}+\int_{\mathcal{S}(t)}\boldsymbol{q}\cdot\boldsymbol{n}(\nabla_{\mathcal{S}(t)}\cdot\boldsymbol{n}). \tag{2.1}$$

For an arbitrary scalar function v, if we take the vector field $\boldsymbol{q}$ tangential to the surface $\mathcal{S}(t)$, namely $\boldsymbol{q}=\nabla_{\mathcal{S}(t)}u$, then we obtain the following Green's formula on the surface $\mathcal{S}(t)$

$$\int_{\mathcal{S}(t)}\nabla_{\mathcal{S}(t)}u\cdot\nabla_{\mathcal{S}(t)}v=\int_{\partial\mathcal{S}(t)}v\nabla_{\mathcal{S}(t)}u\cdot\boldsymbol{\mu}-\int_{\mathcal{S}(t)}v\Delta_{\mathcal{S}(t)}u.$$

Since we consider closed surfaces with no boundary, the surface boundary integral vanishes, and the Green's formula becomes:

$$\int_{\mathcal{S}(t)}v\Delta_{\mathcal{S}(t)}u=-\int_{\mathcal{S}(t)}\nabla_{\mathcal{S}(t)}u\cdot\nabla_{\mathcal{S}(t)}v. \tag{2.2}$$

Let $\boldsymbol{x}\in\mathcal{S}(t)$ be the coordinates on the evolving surface $\mathcal{S}(t)$. Clearly the position $\boldsymbol{x}$ is a function of time and let $\boldsymbol{\beta}$ denotes the material velocity defined as $\frac{d\boldsymbol{x}}{dt}=\boldsymbol{\beta}$. We denote the material derivative of $u(\boldsymbol{x},t)$ by $\dot{u}$ and define it as

$$\dot{u}=\frac{\partial u}{\partial t}+\boldsymbol{\beta}\cdot\nabla_{\mathcal{S}(t)}u. \tag{2.3}$$

By integrating the surface integral over the evolving surface $\mathcal{S}(t)$, we get the following Leibniz formula

$$\frac{d}{dt}\int_{\mathcal{S}(t)}u=\int_{\mathcal{S}(t)}\dot{u}+u\nabla_{\mathcal{S}(t)}\cdot\boldsymbol{\beta}. \tag{2.4}$$

The proof of (2.4) can be found in [13].

Let $\boldsymbol{u}(\boldsymbol{x},t)=\big(u_1(\boldsymbol{x},t),u_2(\boldsymbol{x},t),\cdots,u_m(\boldsymbol{x},t)\big)^T$ be a vector of real valued functions representing chemical concentrations. Suppose that these chemical concentrations diffuse and react on the surface of $\mathcal{S}(t)$. We assume that interactions between chemical species only take place through the nonlinear reaction kinetics identified by the vector function $F(\boldsymbol{u})=(f_1,f_2,\cdots,f_m)^T$. For each chemical concentration we have the mass conservation

https://doi.org/10.4208/cicp.OA-2016-0029 Published online by Cambridge University Press

law which states that for any arbitrary portion, $\Gamma(t)$, of the surface $\mathcal{S}(t)$, the rate of change in the chemical concentration equals to the sum of outward flux through the boundary and the net reaction rate. In mathematical notation, for all $\Gamma(t)\subset\mathcal{S}(t)$

$$\frac{d}{dt}\int_{\Gamma(t)}\boldsymbol{u}=\int_{\partial\Gamma(t)}\boldsymbol{q}\cdot\boldsymbol{\nu}+\int_{\Gamma(t)}F(\boldsymbol{u}), \tag{2.5}$$

where $\boldsymbol{\nu}$ is the unit outward normal to $\partial\Gamma(t)$. We assume that the flux is a tangential vector to the surface, thus we take flux to be $\boldsymbol{q}=D\nabla_{\Gamma(t)}\boldsymbol{u}$, where $D=\mathrm{diag}(d_1,d_2,\cdots,d_m)$ is the diffusion tensor and d_i is the diffusion constant for the chemical concentration u_i. Using Leibniz formula (2.4) we get

$$\int_{\Gamma(t)}\dot{\boldsymbol{u}}+\boldsymbol{u}\nabla_{\Gamma(t)}\cdot\beta=\int_{\partial\Gamma(t)}D\nabla_{\Gamma(t)}\boldsymbol{u}\cdot\boldsymbol{\nu}+\int_{\Gamma(t)}F(\boldsymbol{u}). \tag{2.6}$$

Applying the divergence formula given in (2.1), we replace the boundary surface integral with

$$\int_{\partial\Gamma(t)}D\nabla_{\Gamma(t)}\boldsymbol{u}\cdot\boldsymbol{\nu}=\int_{\Gamma(t)}\nabla_{\Gamma(t)}\cdot D\nabla_{\Gamma(t)}\boldsymbol{u}-\int_{\Gamma(t)}D\nabla_{\Gamma(t)}\boldsymbol{u}\cdot\boldsymbol{n}(\nabla_{\Gamma(t)}\cdot\boldsymbol{n}). \tag{2.7}$$

Noting that $D\nabla_{\Gamma(t)}\boldsymbol{u}\cdot\boldsymbol{n}=0$, the last integral in (2.7) vanishes and Eq. (2.6) becomes

$$\int_{\Gamma(t)}\dot{\boldsymbol{u}}+\boldsymbol{u}\nabla_{\Gamma(t)}\cdot\boldsymbol{\beta}=\int_{\Gamma(t)}D\Delta_{\Gamma(t)}\boldsymbol{u}+\int_{\Gamma(t)}F(\boldsymbol{u}). \tag{2.8}$$

Since (2.8) holds for every $\Gamma(t)$, we get the following system of reaction-diffusion equations defined on the evolving surface $\mathcal{S}(t)$

$$\dot{\boldsymbol{u}}+\boldsymbol{u}\nabla_{\mathcal{S}(t)}\cdot\boldsymbol{\beta}-D\Delta_{\mathcal{S}(t)}\boldsymbol{u}=F(\boldsymbol{u}). \tag{2.9}$$

No boundary conditions are required for the system (2.9) since the surface $\mathcal{S}(t)$ is closed. Initial conditions are prescribed as a positive bounded vector function $\boldsymbol{u}(\boldsymbol{x}(0),0)=\boldsymbol{u}_0(\boldsymbol{x})$. The surface evolution adds two terms to the reaction-diffusion system: $\boldsymbol{\beta}\cdot\nabla_{\mathcal{S}(t)}\boldsymbol{u}$ (hidden in the material derivative (2.3)) and $\boldsymbol{u}\nabla_{\mathcal{S}(t)}\cdot\boldsymbol{\beta}$. The advection term $\boldsymbol{\beta}\cdot\nabla_{\mathcal{S}(t)}\boldsymbol{u}$ represents the movement of the chemical species $\boldsymbol{u}$ with material velocity $\boldsymbol{\beta}$, and the dilution (concentration) term $\boldsymbol{u}\nabla_{\mathcal{S}(t)}\cdot\boldsymbol{\beta}$, which represents dilution (or concentration) of the chemical species due to the increase (or decrease) of the surface volume.

2.1 Surface evolution

First, we introduce the projection operator, $\mathcal{P}$, on closed stationary surfaces which was introduced in [39] for the case of projected finite elements. Next, we describe how this projection can be generalized to take into account surface evolution. The surface evolution law is incorporated into the projection operator, which gives rise to a time-dependent projection operator.

The projection operator, $\mathcal{P}$, is constructed by composing the radial projection $P_{\mathcal{R}}$ with a Lipschitz continuous mapping $\mathcal{T}$. First, let us define the radial projection [31].

https://doi.org/10.4208/cicp.OA-2016-0029 Published online by Cambridge University Press

Definition 2.1. (**Radial projection**) Let B denote a box with side length $2l$, and let $\mathcal{S}_r$ be a sphere with radius r. We denote the radial projection from B onto $\mathcal{S}_r$ by $P_{\mathcal{R}}$ and is defined by

$$P_{\mathcal{R}}(\boldsymbol{x}) = \frac{r\|\boldsymbol{x}\|_\infty}{l\|\boldsymbol{x}\|_2}\boldsymbol{x}. \tag{2.10}$$

Remark 2.1. The radial projection $P_{\mathcal{R}}$ and its inverse $P_{\mathcal{R}}^{-1}$ are Lipschitz continuous [31,38].

Next, we define the projection operator which we use in the projected finite element method.

Definition 2.2. (**Projection operator**) Let $\mathcal{T}$ be a Lipschitz continuous mapping from the sphere $\mathcal{S}_r$ with radius r, to the surface $\mathcal{S}$, whose inverse $\mathcal{T}^{-1}:\mathcal{S}\to\mathcal{S}_r$ is also Lipschitz continuous. Namely, there exist generic constants c and C such that

$$\|\mathcal{T}(\boldsymbol{x}_1)-\mathcal{T}(\boldsymbol{x}_2)\| \le c\|\boldsymbol{x}_1-\boldsymbol{x}_2\|, \tag{2.11}$$

$$\|\mathcal{T}^{-1}(\boldsymbol{y}_1)-\mathcal{T}^{-1}(\boldsymbol{y}_2)\| \le C\|\boldsymbol{y}_1-\boldsymbol{y}_2\|, \tag{2.12}$$

where $\boldsymbol{x}_1,\boldsymbol{x}_2\in\mathcal{S}_r$ and $\boldsymbol{y}_1,\boldsymbol{y}_2\in\mathcal{S}$. The projection operator $\mathcal{P}(\boldsymbol{x})$ is defined by composing the radial projection $P_{\mathcal{R}}$ with the Lipschitz continuous mapping $\mathcal{T}$. That is, $\mathcal{P}:B\to\mathcal{S}$ is

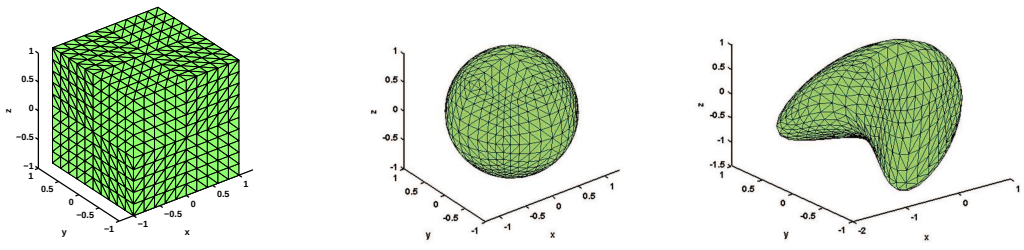
$$\mathcal{P}(\boldsymbol{x}) = (\mathcal{T}\circ P_{\mathcal{R}})(\boldsymbol{x}).$$

Remark 2.2. Note that the projection operator $\mathcal{P}$ and its inverse $\mathcal{P}^{-1}$ are also Lipschitz continuous, since they are constructed by composing Lipschitz continuous mappings.

In Fig. 1 we illustrate an example where a stationary surface, $\mathcal{S}$, is constructed using the projection operator

$$\mathcal{P} = (\mathcal{T}\circ P_{\mathcal{R}})(\boldsymbol{x}) \quad \text{with} \quad \mathcal{T}(x_1,x_2,x_3) = (x_1+x_3^2,x_2,x_3).$$

To study the numerical approximations of reaction-diffusion systems on evolving surfaces, we incorporate the surface evolution into the projection operator $\mathcal{P}$, which yields a time-dependent projection operator.



(a) B (b) $\mathcal{S}_r$ (c) $\mathcal{S}$

Figure 1: Schematic representation of the projection operator $\mathcal{P}$ on stationary surfaces. $P_{\mathcal{R}}:B\to\mathcal{S}_r$ and $\mathcal{T}:\mathcal{S}_r\to\mathcal{S}$. By definition, $\mathcal{P}(\boldsymbol{x})=(\mathcal{T}\circ P_{\mathcal{R}})(\boldsymbol{x})$, hence $\mathcal{P}:B\to\mathcal{S}$. (Color version online).

https://doi.org/10.4208/cicp.OA-2016-0029 Published online by Cambridge University Press

Definition 2.3. (**Time-dependent projection operator**) Let $\mathcal{S}(t)$ denote an evolving surface. Let $\mathcal{T}(\boldsymbol{x},t)$ be a Lipschitz continuous mapping for all $t>0$. $\mathcal{T}(\boldsymbol{x},t)$ is a mapping from the sphere $\mathcal{S}_r$ with radius r, to the surface $\mathcal{S}(t)$, whose inverse $\mathcal{T}^{-1}:\mathcal{S}\to\mathcal{S}_r$ is also Lipschitz continuous for all $t>0$. The surface evolution is determined by the following time-dependent projection operator $\mathcal{P}$

$$\mathcal{P}(\boldsymbol{x},t)=(\mathcal{T}\circ P_{\mathcal{R}})(\boldsymbol{x},t).$$

Hence $\mathcal{P}:B\to\mathcal{S}(t)$. Note that the radial projection $P_{\mathcal{R}}(\boldsymbol{x})$ does not depend explicitly on time, and the mapping $\mathcal{T}(\boldsymbol{x},t)$ is time-dependent. The inverse of time-dependent projector operator is defined as

$$\mathcal{P}^{-1}(\boldsymbol{x},t)=(\mathcal{T}\circ P_{\mathcal{R}})^{-1}(\boldsymbol{x},t).$$

Note that, since the projected operator is composed of two Lipschitz continuous mappings, the time-dependent projection operator $\mathcal{P}(\boldsymbol{x},t)$ as well as its inverse $\mathcal{P}^{-1}(\boldsymbol{x},t)$ are Lipschitz continuous.

Remark 2.3. The quality of the mesh generated by the Lipschitz continuous mappings $\mathcal{P}(\boldsymbol{x})$ have been studied in [31,39]. Since for any fixed time the time-dependent projection operators $\mathcal{P}(\boldsymbol{x},t)$ and $\mathcal{P}^{-1}(\boldsymbol{x},t)$ are Lipschitz continuous, the meshes generated by these projectors are also shape regular. But, clearly the quality of the mesh depends on the Lipschitz constant of the operator $\mathcal{P}(\boldsymbol{x},t)$ (for details see [39]).

Remark 2.4. In all the examples illustrated in this article, we model the time-dependent projection operator $\mathcal{T}$ from hypothetically defined growth functions that are experimentally plausible. In practice, such an operator could be derived from experimental observations through data-fitting.

In the following examples, we demonstrate that isotropic, anisotropic and concentration-driven evolution of closed surfaces can be defined by the time-dependent projection operator $\mathcal{P}(\boldsymbol{x},t)$.

Example 1: Isotropic evolution of the unit sphere

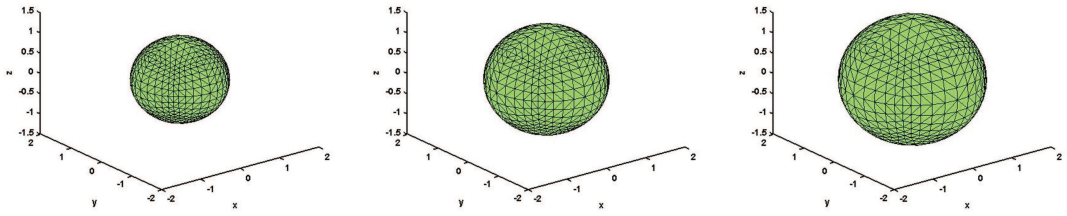
Since the radial projection $P_{\mathcal{R}}$ projects the cube B onto the sphere, we take $r=1$, $l=1$ in (2.10) and take the time-dependent mapping $\mathcal{T}(\boldsymbol{x},t)$ as

$$\mathcal{T}(x_1,x_2,x_3,t)=\rho(t)(x_1,x_2,x_3),$$

where $\rho(t)$ is the following logistic growth function

$$\rho(t)=\frac{Ke^{g_rt}}{(K-1)+e^{g_rt}}. \tag{2.13}$$

https://doi.org/10.4208/cicp.OA-2016-0029 Published online by Cambridge University Press



(a) $t=0$ (b) $t=10$ (c) $t=50$

Figure 2: Isotropic growth of the unit sphere. The growth is given by the time-dependent projection operator $\mathcal{P}(\boldsymbol{x},t)$ as given in *Example 1*. The growth function $\rho(t)$ is a logistic function defined in (2.13). The final size of the radius is $K=1.5$ and the growth rate is $g_r=0.1$. (Color version online).

Here K is the final size of the radius and g_r is the growth rate. The uniform isotropic evolution of the unit sphere, $\mathcal{S}(t)$, is determined by the following projector operator

$$\mathcal{P}(\boldsymbol{x},t)=(\mathcal{T}\circ P_{\mathcal{R}})(\boldsymbol{x},t). \tag{2.14}$$

Fig. 2 shows the uniform isotropic growth of the unit sphere determined by the time-dependent projection operator $\mathcal{P}(\boldsymbol{x},t)$ given in (2.14).

Let $\mathcal{S}_0$ be the initial surface at time $t=0$, that is $\mathcal{S}(0)=\mathcal{S}_0$, and let $\boldsymbol{x}_0\in\mathcal{S}_0$ be the position vector at time $t=0$. Then the uniform isotropic evolution of the surface given by the time-dependent projection operator (2.14) is equivalent to the following

$$\boldsymbol{x}(t)=\rho(t)\boldsymbol{x}_0,$$

where $\boldsymbol{x}(t)$ is the position vector at time t and $\boldsymbol{x}(t)\in\mathcal{S}(t)$. It is clear that for $t=0$, $\mathcal{S}(0)=\mathcal{P}(\boldsymbol{x}(0),0)=\mathcal{P}(\boldsymbol{x}_0)$ and $\mathcal{S}(t)=\mathcal{P}(\boldsymbol{x},t)$.

Next, we consider anisotropic evolution of the surface. Implementation of the time-dependent projection operator on the anisotropic surface evolution is described by the following example.

Example 2: Anisotropic evolution of the dumbbell

Using the time-dependent projection operator, we can define surfaces which exhibit anisotropic evolution. As an example, we present an anisotropic evolution of the dumbbell which is defined by the following time-dependent projection operator

$$\mathcal{P}(\boldsymbol{x},t)=(\mathcal{T}\circ P_{\mathcal{R}})(\boldsymbol{x},t),$$

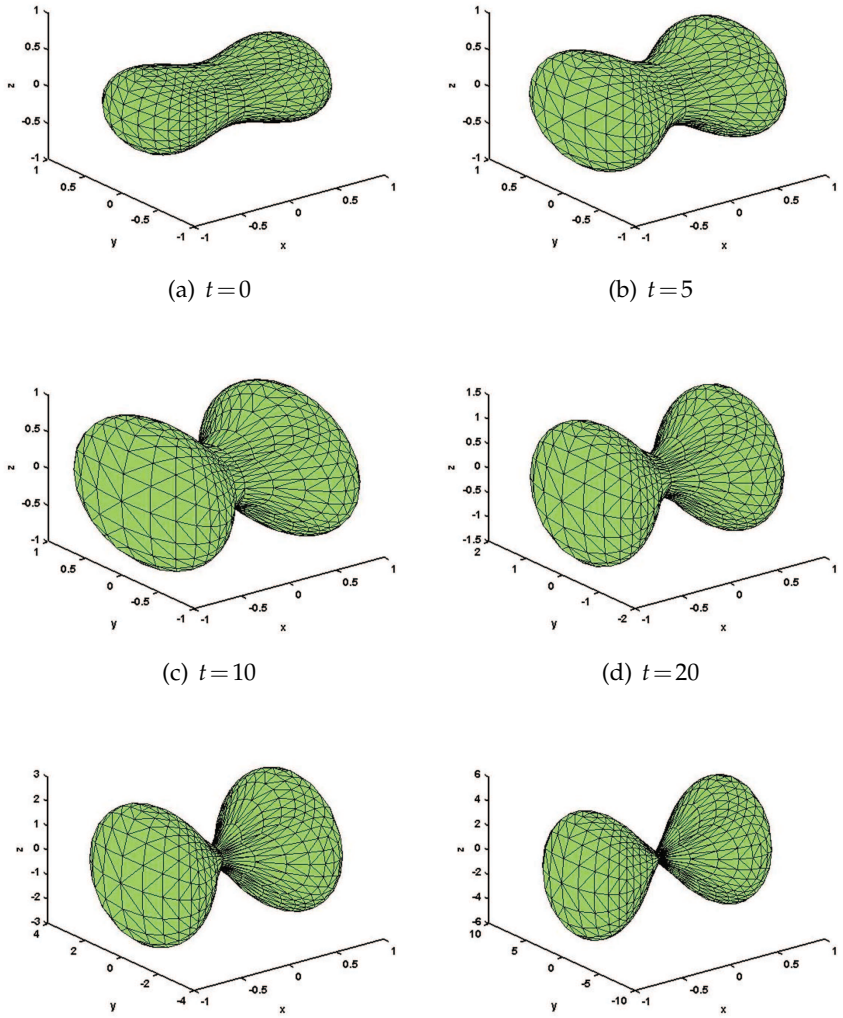
where

$$\mathcal{T}(x_1,x_2,x_3,t)=(x_1,d(x_1,t)x_2,d(x_1,t)x_3)$$

with

$$d(x_1,t)=\sqrt{1-0.85\left(1-(\rho(t)x_1)^2\right)}.$$

https://doi.org/10.4208/cicp.OA-2016-0029 Published online by Cambridge University Press



(a) $t=0$ (b) $t=5$

(c) $t=10$ (d) $t=20$

(e) $t=50$ (f) $t=100$

Figure 3: Anisotropic evolution of the dumbbell. The evolution law is encoded into the time-dependent projection operator $\mathcal{P}(\boldsymbol{x},t)$ (not drawn to scale). (Color version online).

Here, as before, $\rho(t)$ is the growth function (e.g. linear, exponential, logistic). In Fig. 3 the linear form is chosen, thus $\rho(t)=1+\kappa t$ with $\kappa=0.1$.

2.2 Reaction kinetics

To show the robustness and applicability of the projected finite element method for solving systems of reaction-diffusion equations on evolving surfaces, we present the imple-

https://doi.org/10.4208/cicp.OA-2016-0029 Published online by Cambridge University Press

mentation of the methodology to three different reaction kinetics given by the *activator-depleted substrate* [15,34,36], the Gierer-Meinhardt [15] and *activator-activator* [27] models. Below, we describe each model briefly.

2.2.1 *Activator-depleted substrate* reaction kinetics

This is one of the prototype reaction kinetics system. Let $\boldsymbol{u}=(u_1,u_2)$ be a vector of two chemical species. Then the system of reaction-diffusion equations with *activator-depleted substrate* reaction kinetics on an evolving surface $\mathcal{S}(t)$ is given in non-dimensional form [32] by

$$\begin{cases} \dot{u}_1+u_1\nabla_{\mathcal{S}(t)}\cdot\boldsymbol{\beta}-\Delta_{\mathcal{S}(t)}u_1=\gamma(a-u_1+u_1^2u_2), \\ \dot{u}_2+u_2\nabla_{\mathcal{S}(t)}\cdot\boldsymbol{\beta}-d\Delta_{\mathcal{S}(t)}u_2=\gamma(b-u_1^2u_2), \end{cases} \tag{2.15}$$

where a, b and γ are positive parameters. The biological interpretation of the model is that u_1 and u_2 are supplied at constant rates a and b respectively. The negative term $-u_1$ indicates that u_1 is degraded linearly, the positive nonlinear term represents the activation of u_1 and the negative nonlinear term represents the consumption of u_2. In all our simulations, we fix $a=0.1$ and $b=0.9$ and vary d and γ where appropriate.

2.2.2 Gierer-Meinhardt reaction kinetics

This is a phenomenological reaction kinetics of the *activator-inhibitor* form introduced by Gierer-Meinhardt [15] in 1972 and has been widely studied since. In non-dimensional form it can be stated as

$$\begin{cases} \dot{u}_1+u_1\nabla_{\mathcal{S}(t)}\cdot\boldsymbol{\beta}-\Delta_{\mathcal{S}(t)}u_1=\gamma\left(a-bu_1+\dfrac{u_1^2}{u_2(1+K_gu_1^2)}\right), \\ \dot{u}_2+u_2\nabla_{\mathcal{S}(t)}\cdot\boldsymbol{\beta}-d\Delta_{\mathcal{S}(t)}u_2=\gamma\left(u_1^2-u_2\right), \end{cases} \tag{2.16}$$

where u_1 is the activator and u_2 is the inhibitor. The production of the activator u_1 is given by the term $\frac{u_1^2}{u_2(1+K_gu_1^2)}$ which saturates to $\frac{1}{K_gu_2}$ for large u_1. The second equation suggests that the inhibitor u_2 is activated by u_1, but it also inhibits the production of the activator since $\frac{u_1^2}{u_2(1+K_gu_1^2)}$ decreases as u_2 increases. In all our simulations, we fix $a=0.1$, $b=1$ and $K_g=0.5$ and vary d and γ where appropriate.

2.2.3 *Activator-activator* reaction kinetics

In this section we consider a model that violates the cross and/or pure kinetic conditions necessary for the formation of spatial structure on stationary surfaces. These kinetics can give rise to pattern formation only in the presence of surface evolution and were first introduced by Madzvamuse [27] for the case of evolving domains. In non-dimensional form, the system of reaction-diffusion equations on evolving surfaces with

https://doi.org/10.4208/cicp.OA-2016-0029 Published online by Cambridge University Press

activator-activator kinetics takes the form

$$\begin{cases} \dot{u}_1+u_1\nabla_{\mathcal{S}(t)}\cdot\boldsymbol{\beta}-\Delta_{\mathcal{S}(t)}u_1=\gamma\left(\delta(u_1-1)+(u_2-1)+2\delta(u_2-1)^3\right), \\ \dot{u}_2+u_2\nabla_{\mathcal{S}(t)}\cdot\boldsymbol{\beta}-d\Delta_{\mathcal{S}(t)}u_2=\gamma\left(-(u_1-1)+(u_2-1)+(u_2-1)^2-(u_2-1)^3\right), \end{cases} \tag{2.17}$$

where δ is a positive parameter. In all our simulations, we fix $\delta=0.001$ and vary d and γ appropriately.

3 Projected finite element method on evolving surfaces

We apply the projected finite element method to the following generalised reaction-diffusion equation defined on closed evolving surfaces. For $i=1,\cdots,m$,

$$\dot{u}_i+u_i\nabla_{\mathcal{S}(t)}\cdot\boldsymbol{\beta}=d_i\Delta_{\mathcal{S}(t)}u_i+f_i(\boldsymbol{u}). \tag{3.1}$$

3.1 Weak formulation

To get the weak formulation of (3.1), we first multiply by $\omega\in H^1(\mathcal{S}(t))$ and then integrate over the surface $S(t)$. Using (2.2) we obtain

$$\int_{\mathcal{S}(t)}\dot{u}_i\omega+u_i\omega\nabla_{\mathcal{S}(t)}\cdot\beta+\int_{\mathcal{S}(t)}d_i\nabla_{\mathcal{S}(t)}u_i\cdot\nabla_{\mathcal{S}(t)}\omega=\int_{\mathcal{S}(t)}f_i(\boldsymbol{u})\omega.$$

The material derivative of the product of two functions is given by $\dot{(u_i\omega)}=\dot{u}_i\omega+u_i\dot{\omega}$. Thus we can write

$$\int_{\mathcal{S}(t)}\dot{(u_i\omega)}+u_i\omega\nabla_{\mathcal{S}(t)}\cdot\beta-\int_{\mathcal{S}(t)}u_i\dot{\omega}+\int_{\mathcal{S}(t)}d_i\nabla_{\mathcal{S}(t)}u_i\cdot\nabla_{\mathcal{S}(t)}\omega=\int_{\mathcal{S}(t)}f_i(\boldsymbol{u})\omega.$$

Using the Leibniz formula (2.4), we obtain the following weak formulation: Find $u_i\in H^1(\mathcal{S}(t))$ such that

$$\frac{d}{dt}\int_{\mathcal{S}(t)}u_i\omega-\int_{\mathcal{S}(t)}u_i\dot{\omega}+\int_{\mathcal{S}(t)}d_i\nabla_{\mathcal{S}(t)}u_i\cdot\nabla_{\mathcal{S}(t)}\omega=\int_{\mathcal{S}(t)}f_i(\boldsymbol{u})\omega, \tag{3.2}$$

for all $\omega\in H^1(\mathcal{S}(t))$, $i=1,2,\cdots,m$.

3.2 Spatial discretization

To approximate the solutions of the weak formulation (3.2), we construct the finite dimensional subspace $X(t)$ of $H^1(\mathcal{S}(t))$ using the time-dependent projection operator $\mathcal{P}(\boldsymbol{x},t)$. Let K be a planar triangle on the surface of the cube, then the finite element space $X(t)\subset H^1(\mathcal{S}(t))$ is defined as

$X(t)=\{\omega_h:\omega_h=\hat{\omega}\circ\mathcal{P}^{-1}(\boldsymbol{x},t)$, $\hat{\omega}$ is a continuous linear polynomial on B and $\hat{\omega}|_K$ is linear$\}$.

https://doi.org/10.4208/cicp.OA-2016-0029 Published online by Cambridge University Press

The projection operator is used to generate the mesh on $\mathcal{S}(t)$ as follows. Let $\mathcal{K}=\{K_j\}_{j=1}^n$ be a shape regular triangulation of the surface of the cube B. Then the triangulation $\mathcal{T}=\{T_j\}_{j=1}^n$ of the surface $\mathcal{S}(t)$ generated by $\mathcal{T}=\mathcal{P}(\mathcal{K})$ is also shape regular [39].

Let the moving nodal basis functions of $X(t)$ be denoted by $\{\varphi_j(\boldsymbol{x}(t))\}_{j=1}^n$. For the surface triangle T which is constructed by $T=\mathcal{P}(K)$, where K is the planar triangle on the surface of the cube B, let $\{\eta_j\}_{j=1}^3$ be the nodes of the surface triangle T. Let φ_j for $j=1,2,3$ be the basis functions for that surface triangle T, we then define the moving basis functions as

$$\varphi_j(\boldsymbol{x}(t))=\hat{\varphi}_j(\boldsymbol{x})\circ\mathcal{P}^{-1}(\boldsymbol{x},t),\quad j=1,2,3, \tag{3.3}$$

where $\hat{\varphi}_j(\boldsymbol{x})$, $j=1,2,3$, are the linear basis functions for the corresponding planar triangle K. We show that the moving nodal basis functions defined in (3.3) satisfy the following transport property. A similar proof for the transport property of moving basis functions is given in [10].

Proposition 3.1. On $\mathcal{S}(t)$,

$$\dot{\varphi}_j=0 \text{ for } j=1,2,\cdots,n$$

and for any $u=\sum_{j=1}^n\gamma(t)\varphi_j$ we have $\dot{u}=\sum_{j=1}^n\dot{\gamma}(t)\varphi_j$.

Proof. For $j=1,2,3$ let $\varphi_j(\boldsymbol{x}(t))$ be the basis functions for the surface triangle T, and let $\hat{\varphi}_j(\boldsymbol{x})$, $j=1,2,3$, be the linear basis functions for the corresponding planar triangle K (i.e. $T=\mathcal{P}(K)$). Then by definition (3.3) we have

$$\varphi_j(\boldsymbol{x}(t))\circ\mathcal{P}(\boldsymbol{x},t)=\hat{\varphi}_j(\boldsymbol{x}),\quad j=1,2,3. \tag{3.4}$$

Taking the material derivative of both sides of (3.4) leads to $\dot{\varphi}_j=0$ since the material derivative of $\hat{\varphi}_j(\boldsymbol{x})$ is zero [10]. □

We now introduce the discrete weak formulation: Find $\tilde{u}_i\in X(t)$ such that

$$\frac{d}{dt}\int_{\mathcal{S}(t)}\tilde{u}_i\omega_h-\int_{\mathcal{S}(t)}\tilde{u}_i\dot{\omega}_h+\int_{\mathcal{S}(t)}d_i\nabla_{\mathcal{S}(t)}\tilde{u}_i\cdot\nabla_{\mathcal{S}(t)}\omega_h=\int_{\mathcal{S}(t)}f_i(\tilde{\boldsymbol{u}})\omega_h,\quad\forall\omega_h\in X(t). \tag{3.5}$$

Since $\tilde{u}_i\in X(t)$ and $\{\varphi_j\}_{j=1}^n$ is the basis for $X(t)$, there exists $\alpha_i=\{\alpha_i^1,\alpha_i^2,\cdots,\alpha_i^n\}$ such that

$$\tilde{u}_i(\boldsymbol{x},t)=\sum_{j=1}^n\alpha_i^j(t)\varphi_j(\boldsymbol{x}(t)).$$

Taking $\omega_h=\varphi_k$ for $k=1,2,\cdots,n$ in (3.5) and using the transport property of the moving nodal basis functions, we obtain

$$\frac{d}{dt}\int_{\mathcal{S}(t)}\left(\sum_{j=1}^n\alpha_i^j\varphi_j\right)\varphi_k+\int_{\mathcal{S}(t)}d_i\left(\sum_{j=1}^n\alpha_i^j\nabla_{\mathcal{S}(t)}\varphi_j\right)\cdot\nabla_{\mathcal{S}(t)}\varphi_k=\int_{\mathcal{S}(t)}f_i(\tilde{\boldsymbol{u}})\varphi_k. \tag{3.6}$$

https://doi.org/10.4208/cicp.OA-2016-0029 Published online by Cambridge University Press

We rewrite (3.6) in the following compact form

$$\frac{d}{dt}\Big(M(t)\boldsymbol{\alpha}_i(t)\Big)+d_iA(t)\boldsymbol{\alpha}_i(t)=\boldsymbol{F}_i(t), \tag{3.7}$$

where $M(t)$ is the evolving mass matrix with components

$$M(t)_{j,k}=\int_{\mathcal{S}(t)}\varphi_j\varphi_k,$$

$A(t)$ is the evolving stiffness matrix

$$A(t)_{j,k}=\int_{\mathcal{S}(t)}\nabla_{\mathcal{S}(t)}\varphi_j\cdot\nabla_{\mathcal{S}(t)}\varphi_k,$$

and $\boldsymbol{F}_i(t)$ is the right hand side vector

$$(\boldsymbol{F}_i)_{j,k}=\int_{\mathcal{S}(t)}f_i(\tilde{\boldsymbol{u}}_i)\varphi_k.$$

3.3 Time discretization

Let T_m be the final time of interest, τ denotes the time step and let J be a fixed nonnegative integer, then

$$\tau=T_m/J \quad \text{and} \quad t_k=k\tau, \quad \text{with} \quad k=0,1,2,\cdots,J.$$

We represent the approximate solution at time t_k by $\tilde{u}_i^k=\tilde{u}_i(\cdot,t_k)$. We denote by $\mathcal{S}^k=\mathcal{S}(t_k)$ the evolving surface at time t_k and by $\bar{\partial}$ the finite difference operator.

We use the first order time-stepping scheme, and approximate the time-derivative by backward Euler method. Thus

$$\bar{\partial}\tilde{u}_i^k=\frac{\tilde{u}_i^{k+1}-\tilde{u}_i^k}{\tau}. \tag{3.8}$$

Suppose $\tilde{u}_i^0\in X(0)$, and using (3.8) for the time-derivative, then the discrete weak formulation (3.5) becomes

$$\frac{1}{\tau}\int_{\mathcal{S}^{k+1}}\tilde{u}_i^{k+1}\omega_h^{k+1}-\frac{1}{\tau}\int_{\mathcal{S}^k}\tilde{u}_i^k\omega_h^k+\int_{\mathcal{S}^{k+1}}d_i\nabla_{\mathcal{S}^{k+1}}\tilde{u}_i^{k+1}\cdot\nabla_{\mathcal{S}^{k+1}}\omega_h^{k+1}=\int_{\mathcal{S}^{k+1}}f_i(\tilde{\boldsymbol{u}}^{k+1})\omega_h^{k+1}.$$

Rewriting the terms, we get

$$\int_{\mathcal{S}^{k+1}}\tilde{u}_i^{k+1}\omega_h^{k+1}+\tau\int_{\mathcal{S}^{k+1}}d_i\nabla_{\mathcal{S}^{k+1}}\tilde{u}_i^{k+1}\cdot\nabla_{\mathcal{S}^{k+1}}\omega_h^{k+1}-\tau\int_{\mathcal{S}^{k+1}}f_i(\tilde{\boldsymbol{u}}^{k+1})\omega_h^{k+1}=\int_{\mathcal{S}^k}\tilde{u}_i^k\omega_h^k \tag{3.9}$$

for $i=1,2,\cdots,m$.

3.4 Numerical treatment of the different reaction kinetics

To handle the nonlinear terms in reaction kinetics, we use a modified backward Euler introduced in [26]. The first order modified backward Euler method treats the diffusion, growth and linear reaction terms implicitly and nonlinear reaction terms semi-implicitly.

https://doi.org/10.4208/cicp.OA-2016-0029 Published online by Cambridge University Press

3.4.1 *Activator-depleted substrate* reaction kinetics

We now focus on approximating solutions of the system of reaction-diffusion equations with *activator-depleted substrate* reaction kinetics on evolving surfaces using the projected finite elements. We treat the time-derivative by first order backward Euler difference equation given in (3.8). Assuming that the surface evolves slowly, the nonlinear term $u_1^2u_2$ in the reaction kinetics (2.15) is linearized as $\tilde{u}_1^{k+1}\tilde{u}_1^k\tilde{u}_2^k$ where $\tilde{u}_1^k$ is the approximation at time t_k. This is a semi-implicit linearization [26]. Applying the first order modified backward Euler method to the system of reaction-diffusion equations (3.9) we have

$$\begin{aligned}(1+\gamma\tau)\int_{\mathcal{S}^{k+1}}\tilde{u}_1^{k+1}\omega_h^{k+1}+\tau\int_{\mathcal{S}^{k+1}}\nabla_{\mathcal{S}^{k+1}}\tilde{u}_1^{k+1}\cdot\nabla_{\mathcal{S}^{k+1}}\omega_h^{k+1}-\gamma\tau\int_{\mathcal{S}^{k+1}}\tilde{u}_1^k\tilde{u}_2^k\tilde{u}_1^{k+1}\omega_h^{k+1}\\ =\gamma\tau\int_{\mathcal{S}^k}a\omega_h^k+\int_{\mathcal{S}^k}\tilde{u}_1^k\omega_h^k,\end{aligned}\tag{3.10}$$

$$\begin{aligned}\int_{\mathcal{S}^{k+1}}\tilde{u}_2^{k+1}\nu_h^{k+1}+d\tau\int_{\mathcal{S}^{k+1}}\nabla_{\mathcal{S}^{k+1}}\tilde{u}_2^{k+1}\cdot\nabla_{\mathcal{S}^{k+1}}\nu_h^{k+1}-\gamma\tau\int_{\mathcal{S}^{k+1}}(\tilde{u}_1^{k+1})^2\tilde{u}_2^{k+1}\nu_h^{k+1}\\ =\gamma\tau\int_{\mathcal{S}^k}b\nu_h^k+\int_{\mathcal{S}^k}\tilde{u}_2^k\nu_h^k.\end{aligned}\tag{3.11}$$

In the following matrix notation, the evolving mass matrix at time t_{k+1} is denoted as $M^{k+1}=M(t_{k+1})$. Similar notations suffice for the other evolving matrices such as the stiffness matrix. We can then write (3.10) and (3.11) in compact matrix-vector form as

$$\begin{cases}\left((1+\gamma\tau)M^{k+1}+\tau A^{k+1}-\gamma\tau MS_1^{k+1}\right)\boldsymbol{\alpha}_1^{k+1}=\gamma\tau F_1^k+M^k\boldsymbol{\alpha}_1^k,\\ \left(M^{k+1}+d\tau A^{k+1}-\gamma\tau MS_2^{k+1}\right)\boldsymbol{\alpha}_2^{k+1}=\gamma\tau F_2^k+M^k\boldsymbol{\alpha}_2^k,\end{cases}\tag{3.12}$$

where

$$\left(MS_1^{k+1}\right)_{i,j}=\int_{\mathcal{S}^{k+1}}\tilde{u}_1^k\tilde{u}_2^k\varphi_i^{k+1}\varphi_j^{k+1},\quad \left(MS_2^{k+1}\right)_{i,j}=\int_{\mathcal{S}^{k+1}}(\tilde{u}_1^{k+1})^2\varphi_i^{k+1}\varphi_j^{k+1}$$

and

$$\left(F_1^k\right)_j=\int_{\mathcal{S}^k}a\varphi_j^k,\quad \left(F_2^k\right)_j=\int_{\mathcal{S}^k}b\varphi_j^k,$$

with $\varphi_i^k=\varphi_i(\cdot,t_k)$, and $\boldsymbol{\alpha}_i^k$ is the vector of nodal values of the approximation to $\tilde{u}_i^k$.

3.4.2 Gierer-Meinhardt reaction kinetics

After linearizing the nonlinear terms using the first order modified backward Euler method, the fully discrete scheme with Gierer-Meinhardt reaction kinetics is given in the following matrix form

$$\begin{cases}\left((1+\gamma b\tau)M^{k+1}+\tau A^{k+1}-\gamma\tau MG_1^{k+1}\right)\boldsymbol{\alpha}_1^{k+1}=\gamma\tau F_1^k+M^k\boldsymbol{\alpha}_1^k,\\ \left((1+\gamma\tau)M^{k+1}+d\tau A^{k+1}\right)\boldsymbol{\alpha}_2^{k+1}=\gamma\tau FG_1^k+M^k\boldsymbol{\alpha}_2^k,\end{cases}\tag{3.13}$$

https://doi.org/10.4208/cicp.OA-2016-0029 Published online by Cambridge University Press

where

$$\left(MG_1^{k+1}\right)_{i,j}=\int_{\mathcal{S}^{k+1}}\frac{\tilde{u}_1^k}{\tilde{u}_2^k(1+K_g(\tilde{u}_1^k)^2)}\varphi_i^{k+1}\varphi_j^{k+1},\quad\text{and}\quad\left(FG_1^{k+1}\right)_j=\int_{\mathcal{S}^{k+1}}(\tilde{u}_1^{k+1})^2\varphi_j^{k+1}.$$

3.4.3 Activator-activator reaction kinetics

After linearizing the nonlinear terms using the first order modified backward Euler methods, the fully discrete scheme for the *activator-activator* reaction kinetics is given in the following matrix form

$$\begin{cases}\left((1-\gamma\tau)M^{k+1}+\tau A^{k+1}\right)\boldsymbol{\alpha}_1^{k+1}=\gamma\tau FA_1^{k+1}+M^k\boldsymbol{\alpha}_1^k,\\ \left((1-\gamma\tau)M^{k+1}+d\tau A^{k+1}-\gamma\tau MA_1^{k+1}+\gamma\tau MA_2^{k+1}\right)\boldsymbol{\alpha}_2^{k+1}=\gamma\tau FA_2^{k+1}+M^k\boldsymbol{\alpha}_2^k,\end{cases}$$

where

$$\left(MA_1^{k+1}\right)_{i,j}=\int_{\mathcal{S}^{k+1}}(\tilde{u}_2^k-1)\varphi_i^{k+1}\varphi_j^{k+1},\ \left(MA_2^{k+1}\right)_{i,j}=\int_{\mathcal{S}^{k+1}}(\tilde{u}_2^k-1)^2\varphi_i^{k+1}\varphi_j^{k+1},$$

and

$$\begin{aligned}\left(FA_1^{k+1}\right)_j&=\int_{\mathcal{S}^{k+1}}\left((\tilde{u}_2^k-1)+2\delta(\tilde{u}_2^k-1)^3-\delta\right)\varphi_j^{k+1},\\ \left(FA_2^{k+1}\right)_j&=\int_{\mathcal{S}^{k+1}}\left((\tilde{u}_2^k-1)^2-(\tilde{u}_2^k-1)-\tilde{u}_1^{k+1}\right)\varphi_j^{k+1}.\end{aligned}$$

4 Numerical simulations on evolving surfaces

In this section we present several examples to demonstrate the applicability and generality of the numerical methodology. We consider uniform isotropic, anisotropic and concentration-driven surface evolution laws and different reaction kinetics. The initial conditions in all the experiments with reaction kinetics (2.15)-(2.17) are taken to be small random perturbations around their respective uniform steady states. We also highlight the effects of surface evolution, geometry and curvature to pattern formation. In particular, the *activator-activator* reaction kinetics can only give rise to patterns in the presence of surface evolution [27]. These do not satisfy the cross/pure conditions on stationary surfaces. Patterns are therefore induced by surface growth. We reiterate again that this is a non-standard Turing mechanism that gives rise to patterns only during surface evolution.

4.1 Uniform isotropic growth and decay: linear, exponential and logistic

For the first set of examples, we consider uniform isotropic evolution of the surface.

https://doi.org/10.4208/cicp.OA-2016-0029 Published online by Cambridge University Press

Numerical example 1: Logistic-growth of the unit sphere with Gierer-Meinhardt kinetics

Let us take the initial surface, $\mathcal{S}_0$, to be the unit sphere and the evolution function $\rho(t)$ to be of the logistic form previously defined as

$$\rho(t)=\frac{Ke^{g_r t}}{(K-1)+e^{g_r t}} \quad \text{with} \quad K=1.5 \quad \text{and} \quad g_r=0.1.$$

Since $K=1.5$, the unit sphere is evolving to a sphere with final radius equal to 1.5. We approximate solutions of the reaction-diffusion system with Gierer-Meinhardt kinetics (2.16) on an evolving (expanding) sphere with growth rate g_r. The evolution of the unit sphere is determined by the following time-dependent projection operator

$$\mathcal{P}(\boldsymbol{x},t)=(\mathcal{T}\circ P_{\mathcal{R}})(\boldsymbol{x},t), \quad \text{where} \quad \mathcal{T}(\boldsymbol{x},t)=\rho(t)\boldsymbol{x}.$$

The model parameters values are set as $d=84.1573$ and $\gamma=238.16$ which are taken from [29], with time step equal to $\tau=0.005$. The patterns arising from surface evolution with Gierer-Meinhardt kinetics are shown in Fig. 4. Since the patterns for chemical concentrations u_1 and u_2 show symmetry, we only plot the patterns for the chemical concentration u_1. We observe the formation of spots and circular patterns as the surface continues to evolve.

Numerical example 2: Linear contracting sphere with activator-depleted reaction kinetics

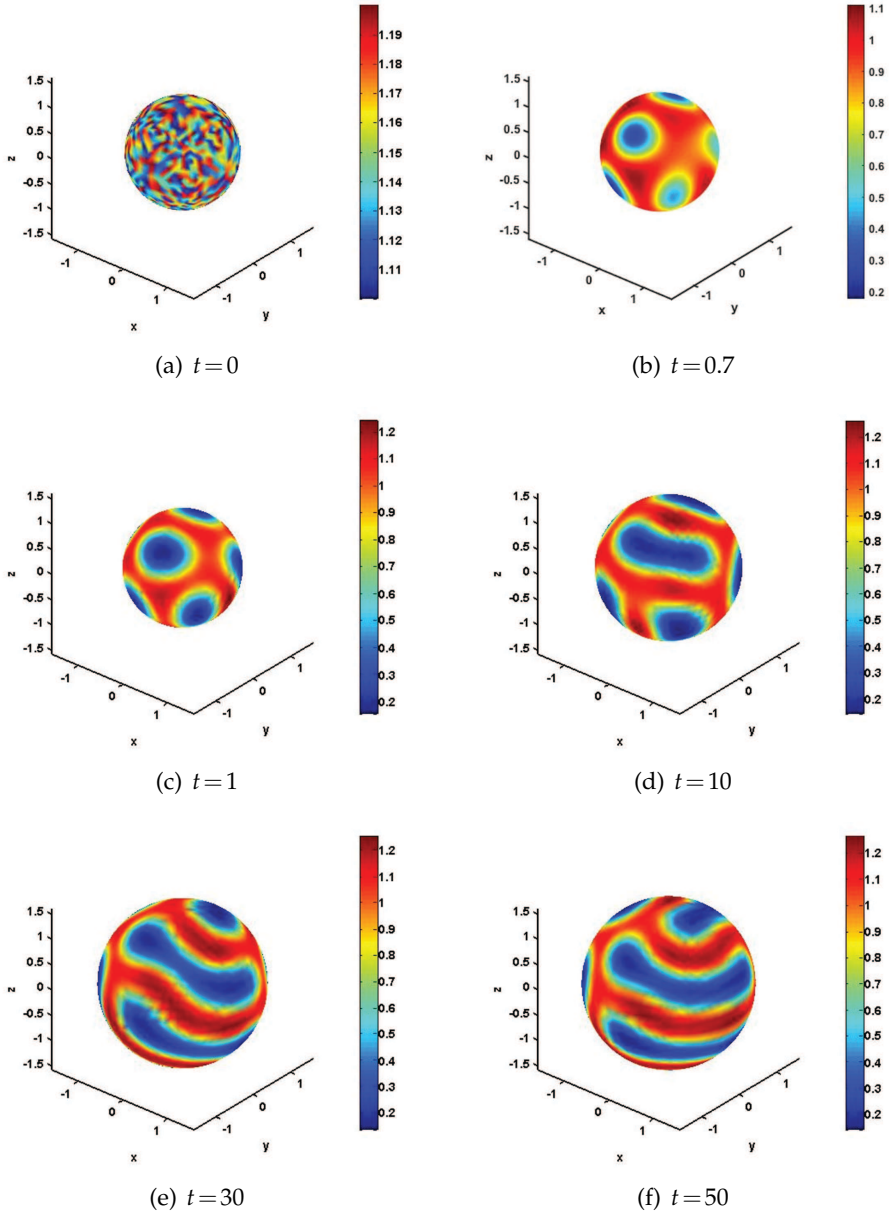
In the second example, we consider surface contraction instead of surface expansion. The initial surface $\mathcal{S}_0$ is the unit sphere which is contracting to a sphere with radius 0.7. The decay is determined by the following time-dependent projection operator

$$\mathcal{P}(\boldsymbol{x},t)=(\mathcal{T}\circ P_{\mathcal{R}})(\boldsymbol{x},t), \quad \text{where} \quad \mathcal{T}(\boldsymbol{x},t)=\rho(t)\boldsymbol{x}, \quad \text{with} \quad \rho(t)=1-g_r t,$$

The sphere is contracting at rate $g_r=0.01$, which is a slower rate compared to the rate in *Numerical example 1*. The final time is set to be 30, hence the final radius is $1-0.01\times 30=0.7$. We approximate the solutions of the reaction-diffusion system with *activator-depleted* reactions (2.15). The patterns arising from a contracting sphere are plotted in Fig. 5.

The model parameter values for this experiment are set to $d=10$ and $\gamma=29$. The time step is equal to $\tau=0.003$. The final pattern on the sphere with radius equal to 0.4 is the same as the pattern forming in *activator-depleted* reaction kinetics on the unit sphere when $\gamma=10$ (see [39]). Hence, this experiment demonstrates that contracting the surface can be thought as decreasing the values of γ without surface evolution. From the random initial conditions, we observe the formation of spots and these evolve into stripe patterns which further evolve into spots as the surface continues to evolve. It is clear that less and less patterns are forming as the surface continues to contract, in contrast to the formation of more patterns when the surface is expanding.

https://doi.org/10.4208/cicp.OA-2016-0029 Published online by Cambridge University Press



(a) $t=0$ (b) $t=0.7$

(c) $t=1$ (d) $t=10$

(e) $t=30$ (f) $t=50$

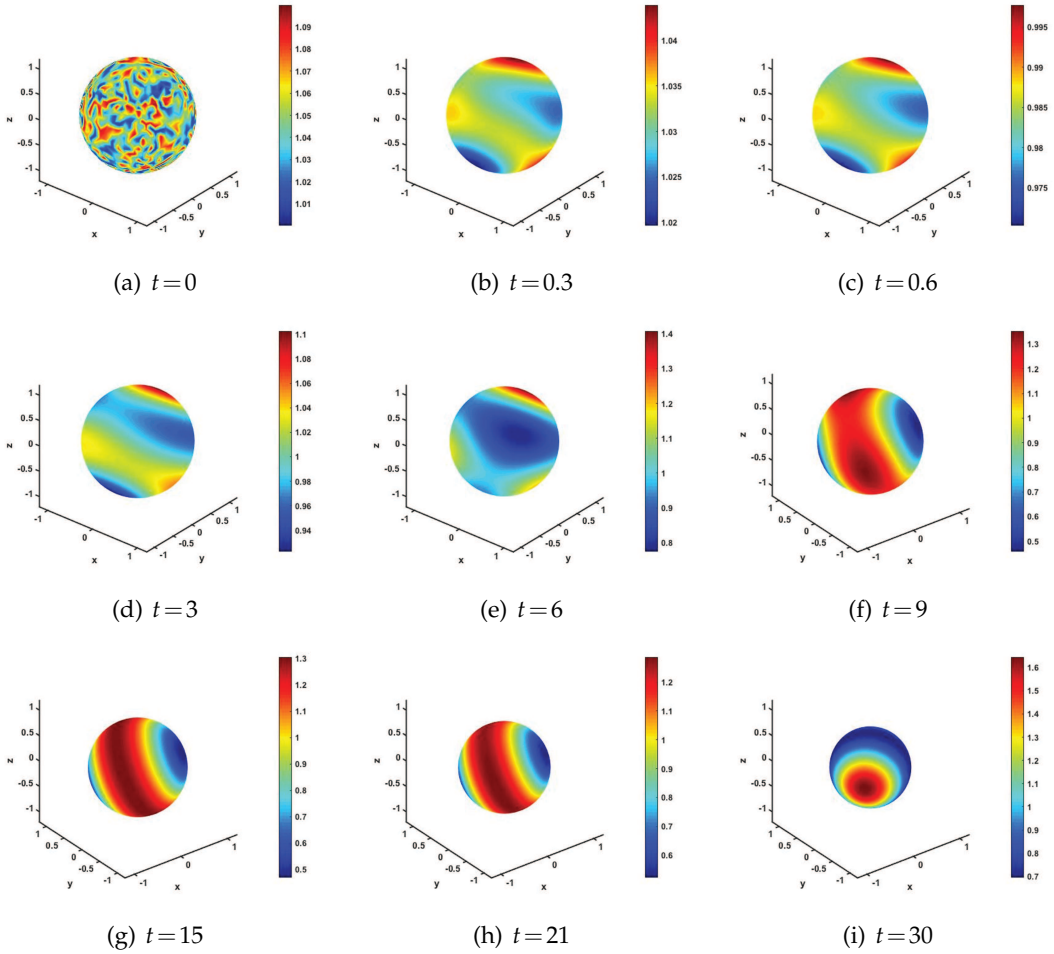
Figure 4: *Numerical example 1:* Patterns arising from the reaction-diffusion system (2.16) on an evolving sphere. These correspond to the u_1 chemical concentration at specific time levels. (Color version online).

Numerical example 3: Exponential growth of heart-shape surface with activator-depleted kinetics

Let $\mathcal{S}(t)$ be an evolving heart-shape surface, whose evolution is determined by the following time-dependent projection operator

$$\mathcal{P}(\boldsymbol{x},t)=(\mathcal{T}\circ P_{\mathcal{R}})(\boldsymbol{x},t),\quad \text{where}\quad \mathcal{T}(x_1,x_2,x_3)=\rho(t)(x_1+x_3^2,x_2,x_3),\quad \text{with}\quad \rho(t)=e^{g_r t}.$$

https://doi.org/10.4208/cicp.OA-2016-0029 Published online by Cambridge University Press



(a) $t=0$ (b) $t=0.3$ (c) $t=0.6$

(d) $t=3$ (e) $t=6$ (f) $t=9$

(g) $t=15$ (h) $t=21$ (i) $t=30$

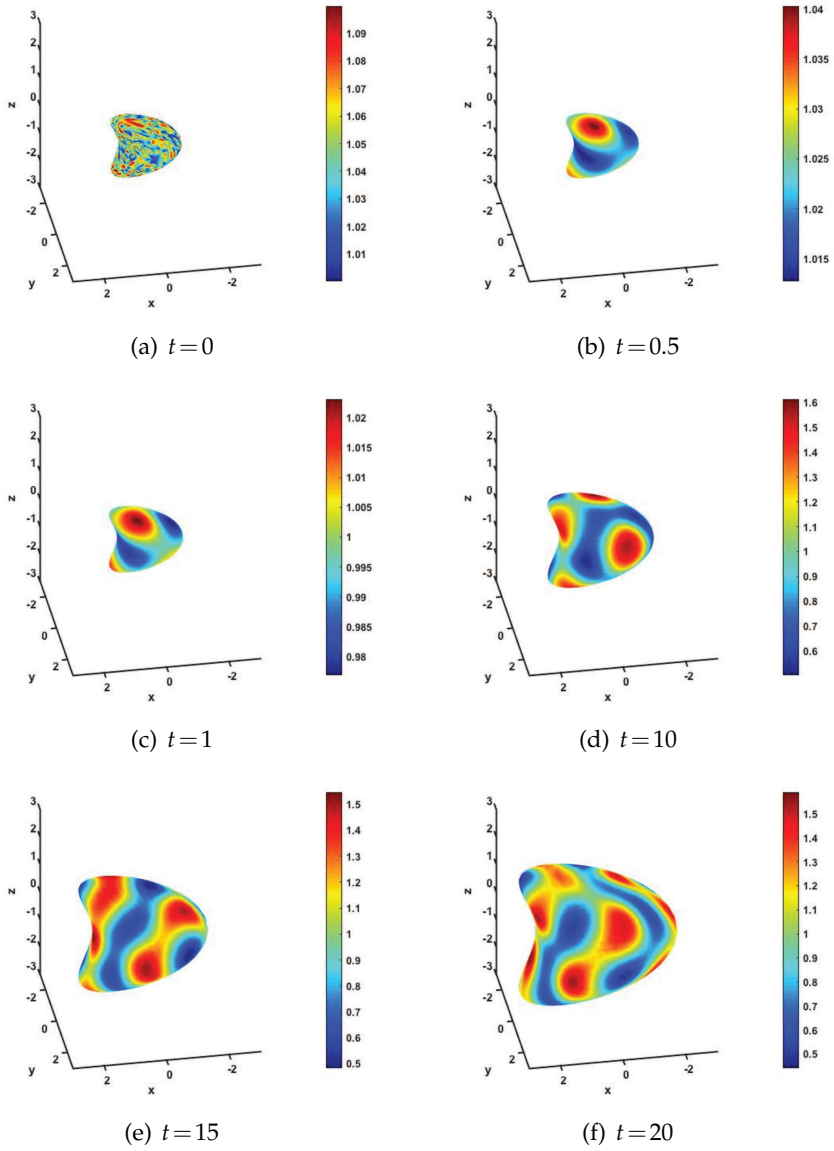
Figure 5: *Numerical example 2:* Patterns arising from the reaction-diffusion system (2.15) on a contracting unit sphere. The figures correspond to the u_1 chemical concentration at specific time levels. (Color version online).

Note that the initial surface $\mathcal{S}_0$ is a heart-shape surface which is constructed by setting $t=0$ in the time-dependent projection operator, thus $\mathcal{P}(\boldsymbol{x},0)$. The model parameters for this experiment are chosen as $d=10$ and $\gamma=29$. The growth rate is set to $g_r=0.04$ and the time step is equal to $\tau=0.002$. We approximate solutions of the reaction-diffusion system with *activator-depleted* kinetics (2.15) on an evolving heart-shape surface. Fig. 6 shows the evolution of patterns with spots evolving into stripes and these into spot patterns as the surface continues to evolve.

Numerical example 4: Exponential evolution of a sphere with activator-activator reaction kinetics

In this example, we approximate the solutions of the reaction-diffusion system with *activator-activator* reaction kinetics (2.17) on an evolving sphere. The evolution of the

https://doi.org/10.4208/cicp.OA-2016-0029 Published online by Cambridge University Press



(a) $t=0$ (b) $t=0.5$

(c) $t=1$ (d) $t=10$

(e) $t=15$ (f) $t=20$

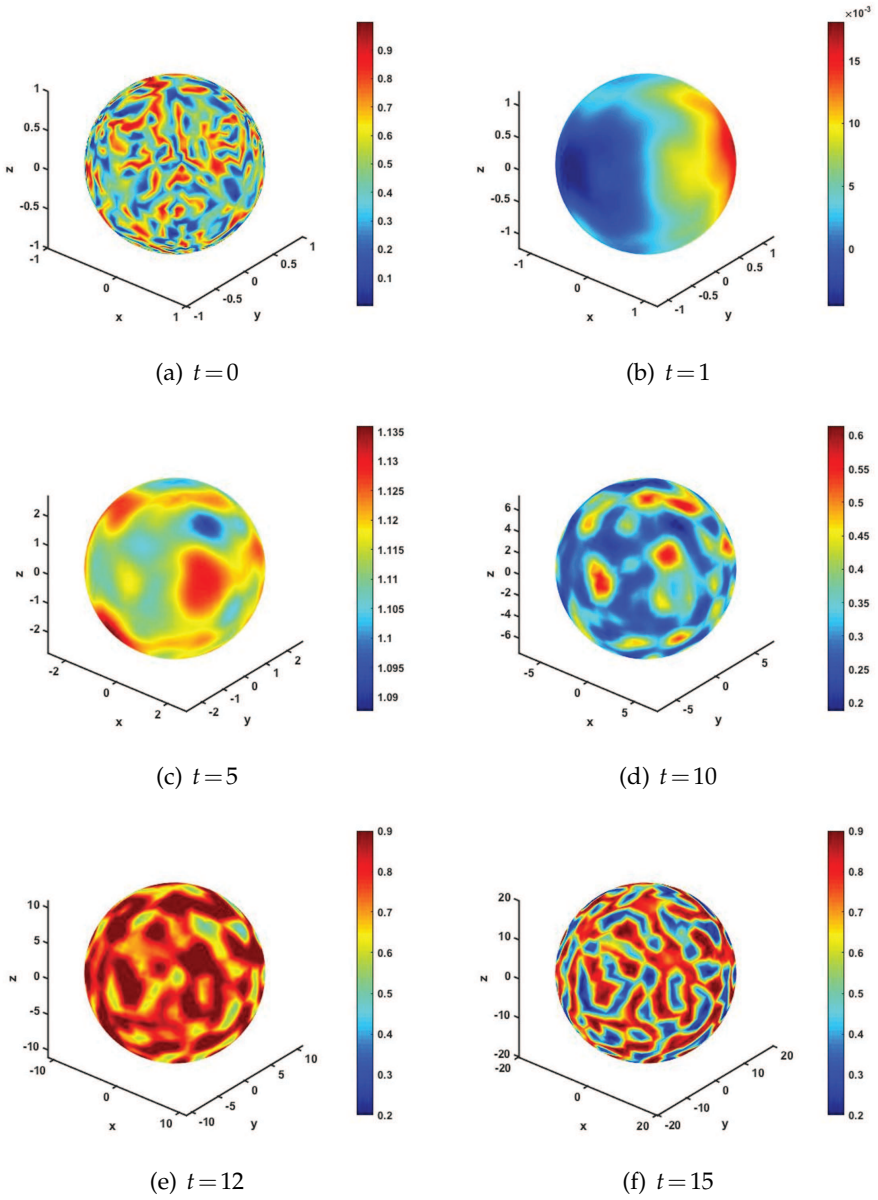
Figure 6: *Numerical example 3:* Patterns arising from the reaction-diffusion system (2.15) on a evolving heart-shape surface. These correspond to the u_1 chemical concentration at specific time levels. (Color version online).

unit sphere is governed by the following projection operator

$$\mathcal{P}(\boldsymbol{x},t)=(\mathcal{T}\circ P_{\mathcal{R}})(\boldsymbol{x},t), \quad \text{where} \quad \mathcal{T}(\boldsymbol{x},t)=\rho(t)\boldsymbol{x}.$$

We consider exponential growth and set $\rho(t)=e^{g_r t}$ with $g_r=0.02$. The parameters for this experiment are set as $d=0.0009$, $\delta=0.001$, and $\gamma=1$. The parameters are taken from [27].

https://doi.org/10.4208/cicp.OA-2016-0029 Published online by Cambridge University Press



(a) $t=0$ (b) $t=1$

(c) $t=5$ (d) $t=10$

(e) $t=12$ (f) $t=15$

Figure 7: *Numerical example 4:* Patterns arising from the reaction-diffusion system with *activator-activator* kinetics (2.17) on an evolving sphere. These correspond to the u_1 chemical concentration at specific time levels. (Color version online).

Fig. 7 shows the evolution of patterns during exponential growth with spots forming from random small perturbations around the critical point (1,1) obtained on a stationary sphere. It must be observed that the *activator-activator* model does not possess stable spatially inhomogeneous solutions on stationary surfaces, but that patterns (transient)

https://doi.org/10.4208/cicp.OA-2016-0029 Published online by Cambridge University Press

form only during growth development [27]. It is an open problem if the *activator-activator* kinetics can give rise to stable spatially inhomogeneous solutions when domain growth is switched off. The patterns exhibited during growth development are constantly evolving and this is an inherent property of pattern formation during growth development (see [29] for further numerical results on growing domains in 2D).

4.2 Anisotropic growth

Numerical example 5: Anisotropic evolution of a sphere into an ellipsoid

In this example, the unit sphere is evolving into an ellipsoid. The anisotropic evolution of the initial surface $\mathcal{S}_0$ is governed by the following time-dependent projection operator

$$\mathcal{P}(\boldsymbol{x},t)=(\mathcal{T}\circ P_{\mathcal{R}})(\boldsymbol{x},t),\quad \text{where}\quad \mathcal{T}(x_1,x_2,x_3,t)=(x_1,x_2,x_3+g_rt).$$

The final time is set to $T_m=50$ and the growth rate is $g_r=0.02$, so that the final surface $\mathcal{S}(T_m)$ is an ellipsoid whose equation is $x_1^2+x_2^2+\frac{2x_3^2}{3}=1$. The solution of the reaction-diffusion system on an evolving surface with *activator-depleted* reaction kinetics is approximated using projected finite element method. The parameters are $d=10$ and $\gamma=200$. The approximate solutions at time $t=0$, 1, 10, 20, 30, 50 are shown in Fig. 8. Here we observe the continuous formation of spots as the surface continues to evolve.

Numerical example 6: An anisotropic evolution of the dumbbell

The anisotropic growth of the dumbbell is determined by the following time-dependent projection operator

$$\mathcal{P}(\boldsymbol{x},t)=(\mathcal{T}\circ P_{\mathcal{R}})(\boldsymbol{x},t), \tag{4.1}$$

where

$$\mathcal{T}(x_1,x_2,x_3,t)=(\rho(t)x_1,d(x_1,t)\rho(t)x_2,d(x_1,t)\rho(t)x_3),$$

with

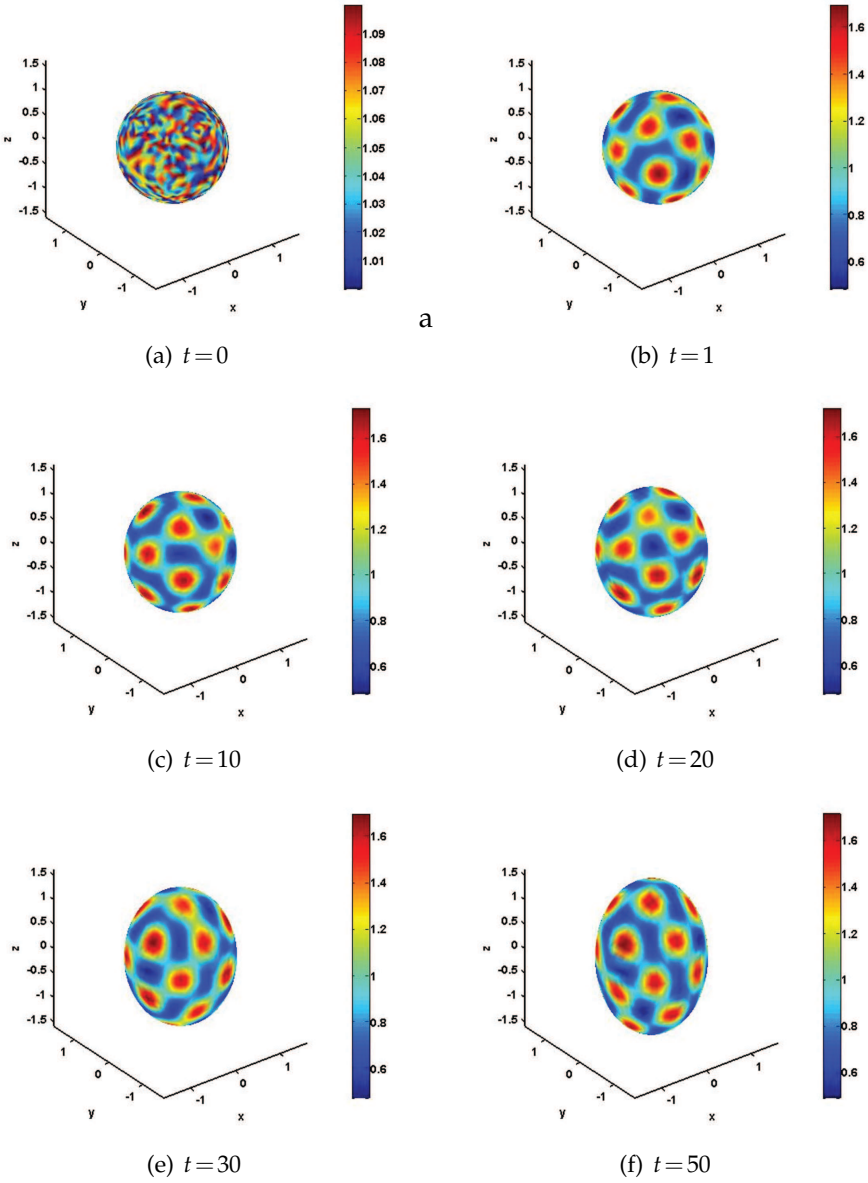
$$d(x_1,t)=\sqrt{1-0.85\left(1-(\rho(t)x_1)^2\right)},\quad \text{and}\quad \rho(t)=1+g_rt.$$

The solutions of the reaction-diffusion system with *activator-depleted* reaction kinetics (2.15) on an evolving surface whose growth is determined by the time-dependent projection operator (4.1) is approximated by the projected finite element method (3.11). The parameters are set as $g_r=0.01$, $d=10$ and $\gamma=60$. The approximate solutions are presented in Fig. 9. We observe some interesting dynamics of the evolution of patterns; stripes and spots forming which are geometrically influenced.

Numerical example 7: Surface evolution driven by chemical concentrations

In this example, we present the effectiveness of the projected finite element method in handling the evolution of the surface which depends on the solution of the reaction-diffusion system. Let the initial surface $\mathcal{S}_0$ be the unit sphere. The evolution law of the

https://doi.org/10.4208/cicp.OA-2016-0029 Published online by Cambridge University Press



(a) $t=0$ (b) $t=1$

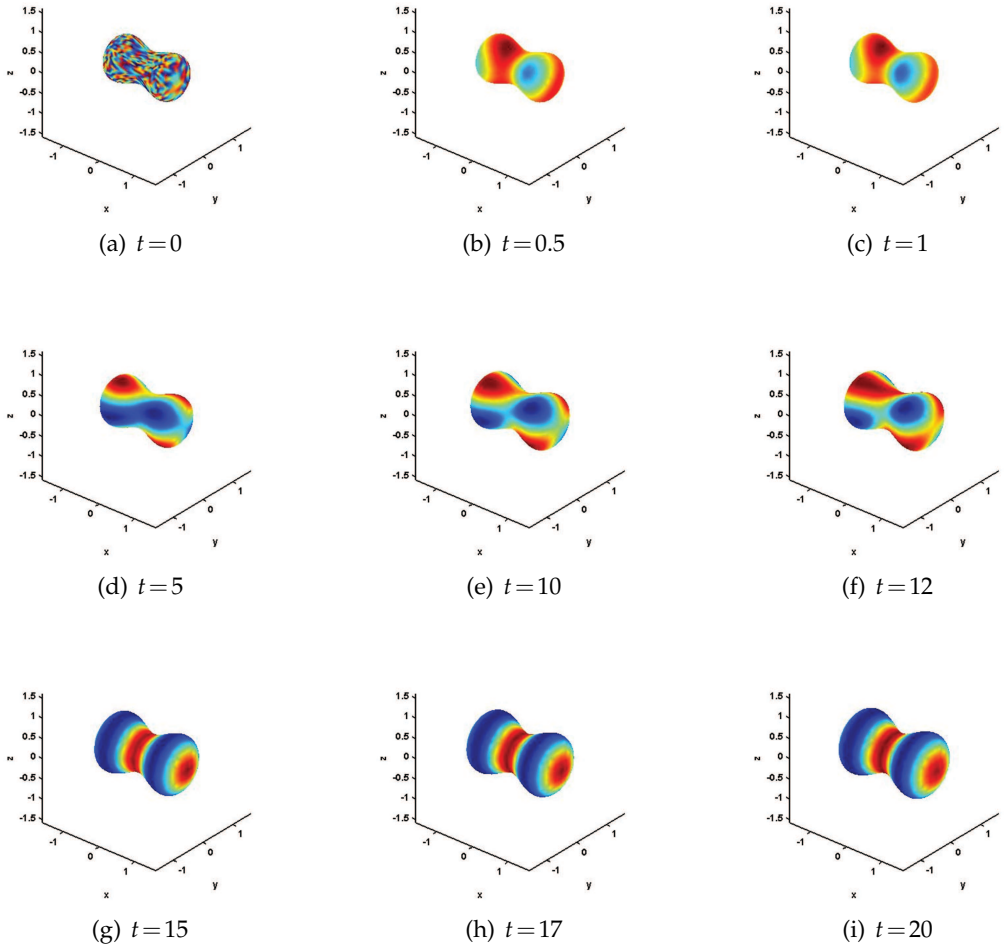
(c) $t=10$ (d) $t=20$

(e) $t=30$ (f) $t=50$

Figure 8: *Numerical example 5:* Patterns arising from the reaction-diffusion system (2.15) on an anisotropic growth of the unit sphere, sphere is evolving into an ellipsoid. These correspond to the u_1 chemical concentration at specific time levels. (Color version online).

sphere is driven by the chemical concentration $u_1(\boldsymbol{x},t)$ in the normal direction which is the solution of the reaction-diffusion system with *activator-depleted* reaction kinetics (2.15). The evolution of the unit sphere is governed by the following time-dependent projection

https://doi.org/10.4208/cicp.OA-2016-0029 Published online by Cambridge University Press



(a) $t=0$ (b) $t=0.5$ (c) $t=1$

(d) $t=5$ (e) $t=10$ (f) $t=12$

(g) $t=15$ (h) $t=17$ (i) $t=20$

Figure 9: *Numerical example 6:* Patterns arising from the reaction-diffusion system (2.15) on an anisotropic growth of the dumbbell, these correspond to the u_1 chemical concentration at specific time levels. (Color version online).

operator

$$\mathcal{P}(\boldsymbol{x},t)=(\mathcal{T}\circ P_{\mathcal{R}})(\boldsymbol{x},t), \tag{4.2}$$

where

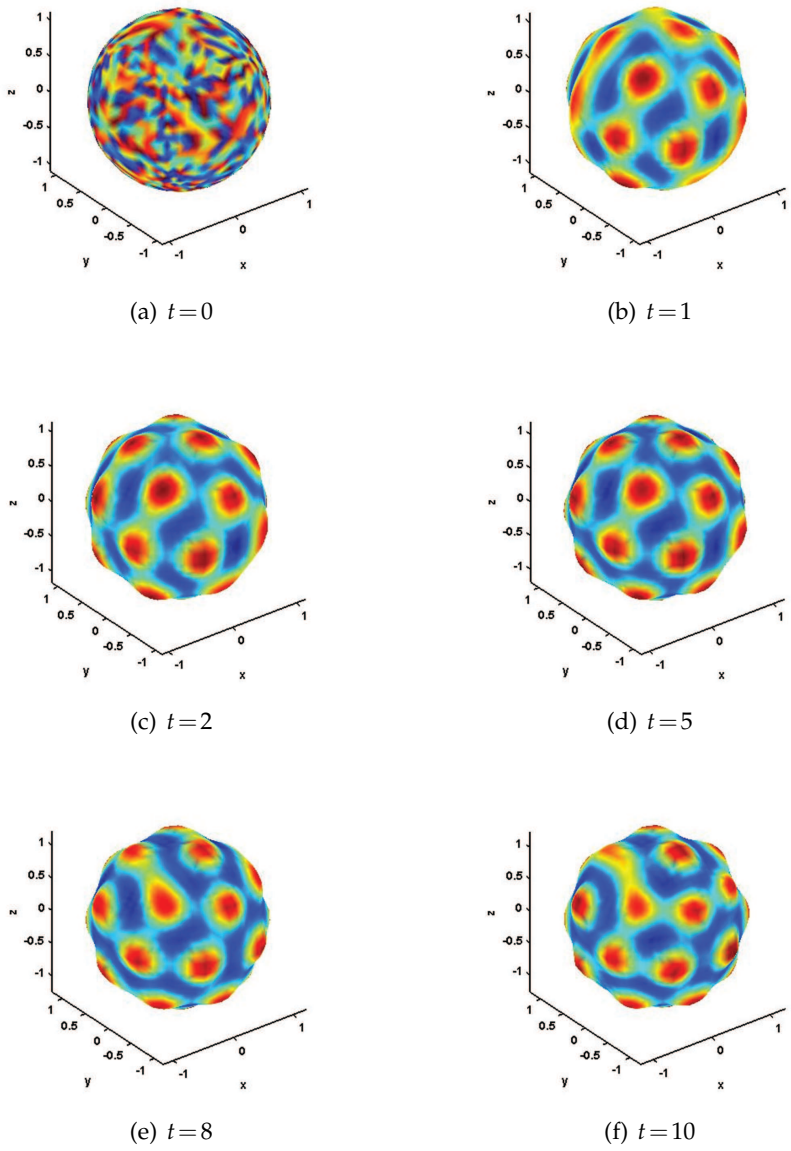
$$\mathcal{T}(x_1,x_2,x_3,t)=(\rho(t)h(\boldsymbol{x},t)x_1,\rho(t)h(\boldsymbol{x},t)x_2,\rho(t)h(\boldsymbol{x},t)x_3),$$

with

$$\rho(t)=1+g_r t \quad \text{and} \quad h(\boldsymbol{x},t)=1+r_h u_1(\boldsymbol{x},t).$$

The solutions of the reaction-diffusion system with *activator-depleted* reaction kinetics (2.15) on an evolving surface whose growth is determined by the (4.2) is approximated

https://doi.org/10.4208/cicp.OA-2016-0029 Published online by Cambridge University Press



(a) $t=0$ (b) $t=1$

(c) $t=2$ (d) $t=5$

(e) $t=8$ (f) $t=10$

Figure 10: *Numerical example 7:* Patterns arising from the reaction-diffusion system (2.15) in which the surface evolution is determined by the chemical concentration as given in (4.2). These correspond to the u_1 chemical concentration at the specified time levels. (Color version online).

by the projected finite element method (3.11). The parameters are set as $g_r = 0.01$, $r_h = 0.1$, $d = 10$ and $\gamma = 200$. The approximate solutions are presented in Fig. 10. Again, we observe the continuous evolution of spot patterns during surface evolution.

https://doi.org/10.4208/cicp.OA-2016-0029 Published online by Cambridge University Press

Numerical example 8: Effect of surface evolution on pattern formation

In this example, we compare the patterns formed when an sphere evolves into two different geometrical surfaces. In both simulations, we approximate the solutions of the reaction-diffusion system with *activator-depleted* reaction kinetics (2.15) on an evolving unit sphere using projected finite element method. In the first simulation, the unit sphere is evolving into a heart-shaped surface, and in the second simulation the unit sphere is evolving to a dumbbell.

The evolution of the unit sphere to heart-shape surface is given by the following time dependent projection operator

$$\mathcal{P}(\boldsymbol{x},t)=(\mathcal{T}\circ P_{\mathcal{R}})(\boldsymbol{x},t),\quad \text{where}\quad \mathcal{T}(x_1,x_2,x_3,t)=(x_1+g_r t x_3^2,x_2,x_3). \tag{4.3}$$

The growth rate is chosen to be $g_r=0.05$. The final time is $T_m=20$, thus the surface at the final time, $\mathcal{S}(T_m)$, can be represented by the equation $(x_1-x_3^2)^2+x_2^2+x_3^2=1$.

The evolution law of the unit sphere to dumbbell is given by the following time dependent projection operator

$$\mathcal{P}(\boldsymbol{x},t)=(\mathcal{T}\circ P_{\mathcal{R}})(\boldsymbol{x},t),\quad \text{where}\quad \mathcal{T}(x_1,x_2,x_3,t)=(x_1,d(x_1)x_2,d(x_1)x_3), \tag{4.4}$$

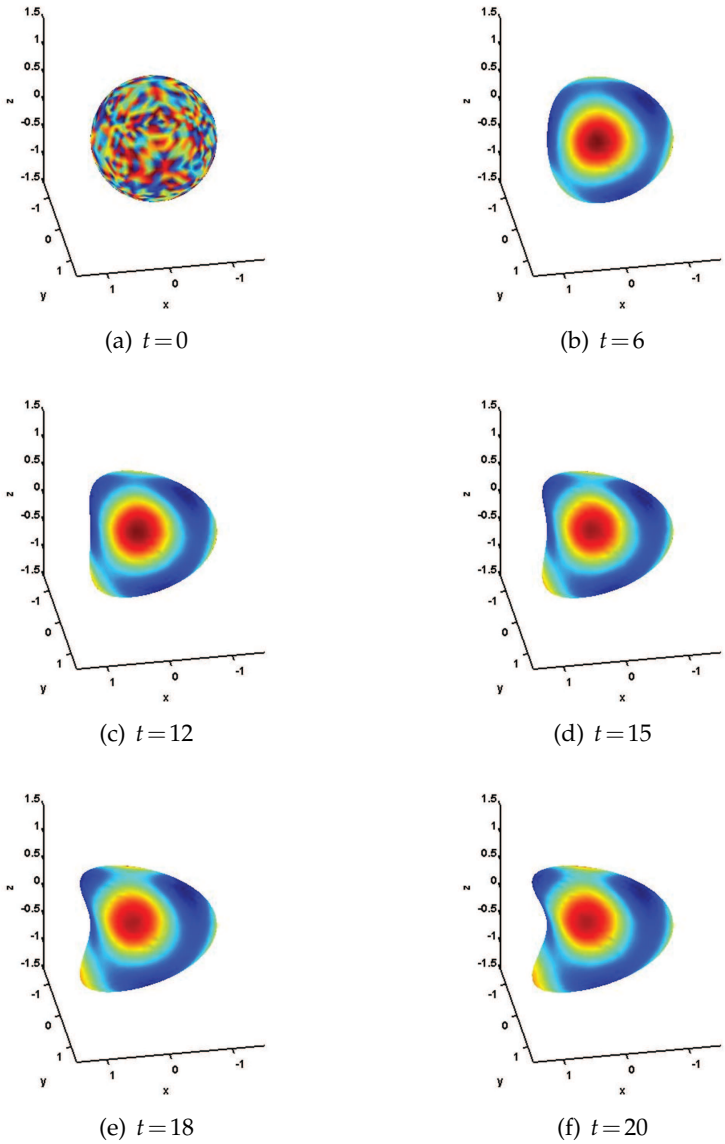
with $d(x_1)=\sqrt{1-g_r t(1-x_1)^2}$. The growth rate is chosen to be same, hence $g_r=0.05$. Note that only at the final time $T_m=20$, $d(x_1)=0$ when $x_1=0$.

In both simulations parameters are set as $d=10$ and $\gamma=29$. The approximate solutions are presented in Figs. 11 and 12. It is clear that pattern evolution is dependent on the geometrical evolution of the surface, we observe different patterns forming during the evolution of the heart-shaped surface versus the formation of the dumbbell. Spots form on the heart-shaped surface while stripes form on the dumbbell. We have taken the same model and numerical parameter values.

5 Conclusion, discussion and future directions

Recent advances in experimental sciences and the rapid exponential increase in computational power necessitate the development of new highly efficient, robust and applicable numerical methods for solving highly nonlinear partial differential models on evolving surfaces and manifolds [1, 13, 24, 39]. In this paper, we have developed a new finite element method, inspired by the radially projected operators, that allows us to solve efficiently and robustly a system of reaction-diffusion equations posed on evolving closed spheroidal surfaces. The projected finite element method on evolving surfaces and manifolds is constructed by composing a time-dependent projection operator with a Lipschitz continuous mapping. The surface evolution law is prescribed explicitly through the projection operator. Examples of surface evolution laws includes linear uniform isotropic (e.g. linear, exponential, logistic), anisotropic and concentration-driven. The latter is particular relevant in cellular biology where experimental evidences show that cell-surface membrane evolution is driven by chemical concentrations resident on the cell surface [5].

https://doi.org/10.4208/cicp.OA-2016-0029 Published online by Cambridge University Press



(a) $t=0$ (b) $t=6$

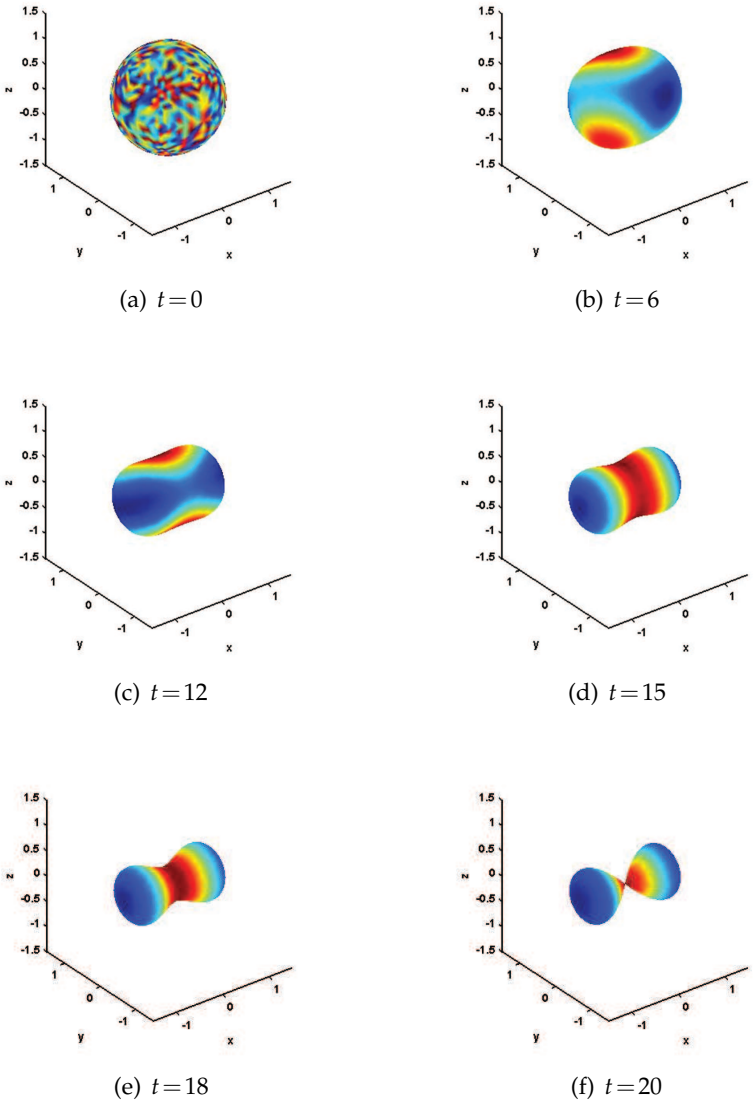
(c) $t=12$ (d) $t=15$

(e) $t=18$ (f) $t=20$

Figure 11: *Numerical example 8:* Patterns arising from the reaction-diffusion system (2.15) in which the unit sphere is evolving into a heart-shaped surface as given in (4.3). These correspond to the u_1 chemical concentration at the specified time levels. (Color version online).

Our results seem to suggest that surface geometry plays an important role in pattern formation, and that further analytical studies are required to study the effects of curvature on pattern formation during growth development. Under such studies, it will be revealing to compare pattern formation on static surfaces to that obtained on closed evolving surfaces. Comparisons of this nature have been undertaken in earlier studies

https://doi.org/10.4208/cicp.OA-2016-0029 Published online by Cambridge University Press



(a) $t=0$ (b) $t=6$

(c) $t=12$ (d) $t=15$

(e) $t=18$ (f) $t=20$

Figure 12: *Numerical example 8:* Patterns arising from the reaction-diffusion system (2.15) in which the unit sphere is evolving into a dumbbell as given in (4.4). These correspond to the u_1 chemical concentration at the specified time levels. (Color version online).

for pattern formation on growing planar domains [29]. By taking a fixed set of model parameter values and varying only the surfaces, we observe the emergence of different patterns and these seem to be driven by both surface geometry and evolution. Different surface evolution laws give rise to different patterns ranging from spots to stripes and a combination of these through circular patterns. Furthermore, surface growth is shown to

https://doi.org/10.4208/cicp.OA-2016-0029 Published online by Cambridge University Press

give rise to the continuous formation of patterns while surface contraction gives rise to pattern annihilation. These results confirm theoretical and computational results for the case of 2-dimensional contracting and expanding domains (see [21] for further details). We also observe different patterns when surfaces are deformed into different geometrical surfaces (e.g. a sphere evolving into an ellipsoidal or dumbbell surface).

By introducing surface evolution a non-standard Turing model with *activator-activator* kinetics is shown to generate patterns only in the presence of surface evolution. Such a model is not capable of giving rise to patterning if the surface is taken stationary since the model violates the necessary conditions for diffusion-driven instability on stationary surfaces [27]. However, by introducing domain growth, an evolving Turing parameter space (i.e. the Turing diffusion-driven instability parameter space is time-dependent [27, 28]) emerges from which patterning can arise only due to surface evolution. Our results confirm theoretical predictions published on evolving domains (see [27] for details).

Although our studies have been restricted to closed evolving spheroidal surfaces, the methodology can be easily extended to open evolving spheroidal surfaces. Here, one could simply assume either homogeneous Neumann boundary conditions (to reflect pattern self-organisation) or homogenous Dirichlet boundary conditions. Other types of boundary conditions such as Robin-type could be studied at the expense of integrating along the boundary of the given open surface. However, it must be noted that defining mappings and projections for such surfaces is a formidable challenge.

Our numerical framework allows us to tackle new experimentally driven models where we will couple surface reaction-diffusion systems to reaction-diffusion type models in the bulk of the surface with applications to cell motility. In cellular biology, cell movement and deformation is observed to be driven by proteins (e.g. actin, myosin, melanin) resident on the cell surface as well as by the dynamics resulting from interactions between cell-surface resident proteins and those residing in the cell interior. Furthermore, coupling the reaction-diffusion models to visco-elastic type models in the bulk of the cell will provide biologists with integrative computational frameworks useful to study interactions such as ligand-receptor reactions.

Acknowledgments

The author N. Tuncer acknowledges support from the National Science Foundation (NSF) under grant DMS-1515442. This work (AM) is partly supported by the EPSRC grant number EP/J016780/1 and the Leverhulme Trust Research Project Grant (RPG-2014-149). AM acknowledges funding from the European Union Horizon 2020 research and innovation programme under the Marie Sklodowska-Curie grant agreement No 642866. The authors (NT, AM) would like to thank the Isaac Newton Institute for Mathematical Sciences for its hospitality during the programme [Coupling Geometric PDEs with Physics for Cell Morphology, Motility and Pattern Formation] supported by EPSRC Grant Number EP/K032208/1 and were partially supported by a grant from the Simons Foundation.

https://doi.org/10.4208/cicp.OA-2016-0029 Published online by Cambridge University Press

References

[1] R. Barreira, C. M. Elliott, and A. Madzvamuse. The surface finite element method for pattern formation on evolving biological surfaces. *J. Math. Biol.*, 63(6):1095–1119, 2011.

[2] K. Blazakis, C. R. Aldasoro, C. Venkataraman, V. Styles, and A. Madzvamuse. An optimal control approach for neutrophil cell motility. *In preparation*.

[3] G. Caginalp. Stefan and Hele-Shaw type models as asymptotic limits of the phase-field equations. *Phys. Rev. A (3)*, 39(11):5887–5896, 1989.

[4] M. A. J. Chaplain, M. Ganesh, and I. G. Graham. Spatio-temporal pattern formation on spherical surfaces: numerical simulation and application to solid tumour growth. *J. Math. Biol.*, 42(5):387–423, 2001.

[5] Y. F. Dagdas, K. Yoshino, G. Dagdas, L. S. Ryder, E. Bielska, G. Steinberg, and N. J. Talbot. Septin-mediated plant cell invasion by the rice blast fungus, magnaporthe oryzae. *Science*, 336(6088):1590–1595, 2012.

[6] K. Deckelnick, G. Dziuk, and C. M. Elliott. Computation of geometric partial differential equations and mean curvature flow. *Acta Numer.*, 14:139–232, 2005.

[7] A. Donna and C. Helzel. A finite volume method for solving parabolic equations on logically Cartesian curved surface meshes. *SIAM J. Sci. Comput.*, 31(6):4066–4099, 2009.

[8] G. Dziuk and C. M. Elliott. Finite elements on evolving surfaces. *IMA J. Numer. Anal.*, 27(2):262–292, 2007.

[9] G. Dziuk and C. M. Elliott. Surface finite elements for parabolic equations. *J. Comput. Math.*, 25(4):385–407, 2007.

[10] G. Dziuk and C. M. Elliott. Surface finite elements for parabolic equations. *J. Comput. Math.*, 25(4):385–407, 2007.

[11] G. Dziuk and C. M. Elliott. Eulerian finite element method for parabolic PDEs on implicit surfaces. *Interfaces Free Bound.*, 10(1):119–138, 2008.

[12] G. Dziuk and C. M. Elliott. An Eulerian approach to transport and diffusion on evolving implicit surfaces. *Comput. Vis. Sci.*, 13(1):17–28, 2010.

[13] G. Dziuk and C. M. Elliott. Finite element methods for surface PDEs. *Acta Numer.*, 22:289–396, 2013.

[14] C. M. Elliott, B. Stinner, V. Styles, and R. Welford. Numerical computation of advection and diffusion on evolving diffuse interfaces. *IMA J. Numer. Anal.*, 31(3):786–812, 2011.

[15] A. Gierer and H. Meinhardt. Theory of biological pattern formation. *Kybernetik*, 12(1):30–39, 1972.

[16] J. B. Greer, A. L. Bertozzi, and G. Sapiro. Fourth order partial differential equations on general geometries. *J. Comput. Phys.*, 216(1):216–246, 2006.

[17] G. Hetzer, A. Madzvamuse, and W. Shen. Characterization of Turing diffusion-driven instability on evolving domains. *Discrete Contin. Dyn. Syst.*, 32(11):3975–4000, 2012.

[18] S. E. Hieber and P. Koumoutsakos. A Lagrangian particle level set method. *J. Comput. Phys.*, 210(1):342–367, 2005.

[19] V. Kadirkamanathan, S. Anderson, S. Billings, X. Zhang, and G. Holmes. The neutrophil's eye-view: Inference and visualisation of the chemoattractant field driving cell chemotaxis in vivo. *PLoS ONE*, 7(4):e35182, 2012.

[20] S. Kondo and R. Asai. A reaction-diffusion wave on the skin of the marine angelfish pomacanthus. *Nature*, 376(6543):765–768, 1995.

[21] O. Lakkis, A. Madzvamuse, and C. Venkataraman. Implicit–explicit timestepping with finite element approximation of reaction–diffusion systems on evolving domains. *SIAM Journal*

https://doi.org/10.4208/cicp.OA-2016-0029 Published online by Cambridge University Press

on Numerical Analysis, 51(4):2309–2330, 2013.
[22] J. Lefèvre and J.-F. Mangin. A reaction-diffusion model of human brain development. *PLoS Comput. Biol.*, 6(4):e1000749, 2010.
[23] S. S. Liaw, C. C. Yang, R. T. Liu, and J. T. Hong. Turing model for the patterns of lady beetles. *Phys. Rev. E.*, 64:041909, 2001.
[24] C. B. Macdonald, B. Merriman, and S. J. Ruuth. Simple computation of reaction-diffusion processes on point clouds. *Proc. Natl. Acad. Sci. USA*, 110(23):9209–9214, 2013.
[25] C. B. Macdonald and S. J. Ruuth. The implicit closest point method for the numerical solution of partial differential equations on surfaces. *SIAM J. Sci. Comput.*, 31(6):4330–4350, 2009/10.
[26] A. Madzvamuse. Time-stepping schemes for moving grid finite elements applied to reaction-diffusion systems on fixed and growing domains. *J. Comput. Phys.*, 214(1):239–263, 2006.
[27] A. Madzvamuse, E. A. Gaffney, and P. K. Maini. Stability analysis of non-autonomous reaction-diffusion systems: the effects of growing domains. *J. Math. Biol.*, 61(1):133–164, 2010.
[28] A. Madzvamuse, H. S. Ndakwo, and R. Barreira. Stability analysis of reaction-diffusion models on evolving domains: the effects of cross-diffusion. *Discrete and Continuous Dynamical Systems - Series A*, 34(4):2133–2170, 2016.
[29] A. Madzvamuse, A. J. Wathen, and P. K. Maini. A moving grid finite element method applied to a model biological pattern generator. *J. Comput. Phys.*, 190(2):478–500, 2003.
[30] H. Meinhardt. *The Algorithmic Beauty of Sea Shells*. The Virtual Laboratory. Springer-Verlag, Berlin, 1995.
[31] A. J. Meir and N. Tuncer. Radially projected finite elements. *SIAM J. Sci. Comput.*, 31(3):2368–2385, 2009.
[32] J. D. Murray. *Mathematical biology. II*, volume 18 of *Interdisciplinary Applied Mathematics*. Springer-Verlag, New York, third edition, 2003. Spatial models and biomedical applications.
[33] S. Osher and R. Fedkiw. *Level set methods and dynamic implicit surfaces*, volume 153 of *Applied Mathematical Sciences*. Springer-Verlag, New York, 2003.
[34] I. Prigogine and R. Lefever. Symmetry breaking instabilities in dissipative systems II. *J. Chem. Phys.*, 48:1695–1700, 1968.
[35] L. Ramms, G. Fabris, R. Windoffer, N. Schwarz, R. Springer, C. Zhou, J. Lazar, S. Stiefel, N. Hersch, U. Schnakenberg, T. M. Magin, R. E. Leube, R. Merkel, and B. Hoffmann. Keratins as the main component for the mechanical integrity of keratinocytes. *Proceedings of the National Academy of Sciences*, 110(46):18513–18518, 2013.
[36] J. Schnakenberg. Simple chemical reaction systems with limit cycle behavior. *J. Theoret. Biol.*, 81(3):389–400, 1979.
[37] J. A. Sethian. *Level set methods and fast marching methods*, volume 3 of *Cambridge Monographs on Applied and Computational Mathematics*. Cambridge University Press, Cambridge, second edition, 1999. Evolving interfaces in computational geometry, fluid mechanics, computer vision, and materials science.
[38] N. Tuncer. *A novel finite element discretization of domains with spheroidal geometry*. Ph.D. Dissertation, Auburn University Libraries, 2007.
[39] N. Tuncer, A. Madzvamuse, and A. J. Meir. Projected finite elements for reaction-diffusion systems on stationary closed surfaces. *Applied and Numerical Mathematics*, 96:45–71, 2015.

https://doi.org/10.4208/cicp.OA-2016-0029 Published online by Cambridge University Press